Mechanical and Structural Characterisation of a Calcified Scaffold

Towards the Development of an
In-Vitro Model of an Atherosclerotic Fibrous Cap

Amal Mansoor

MSc Thesis
Biomedical Engineering

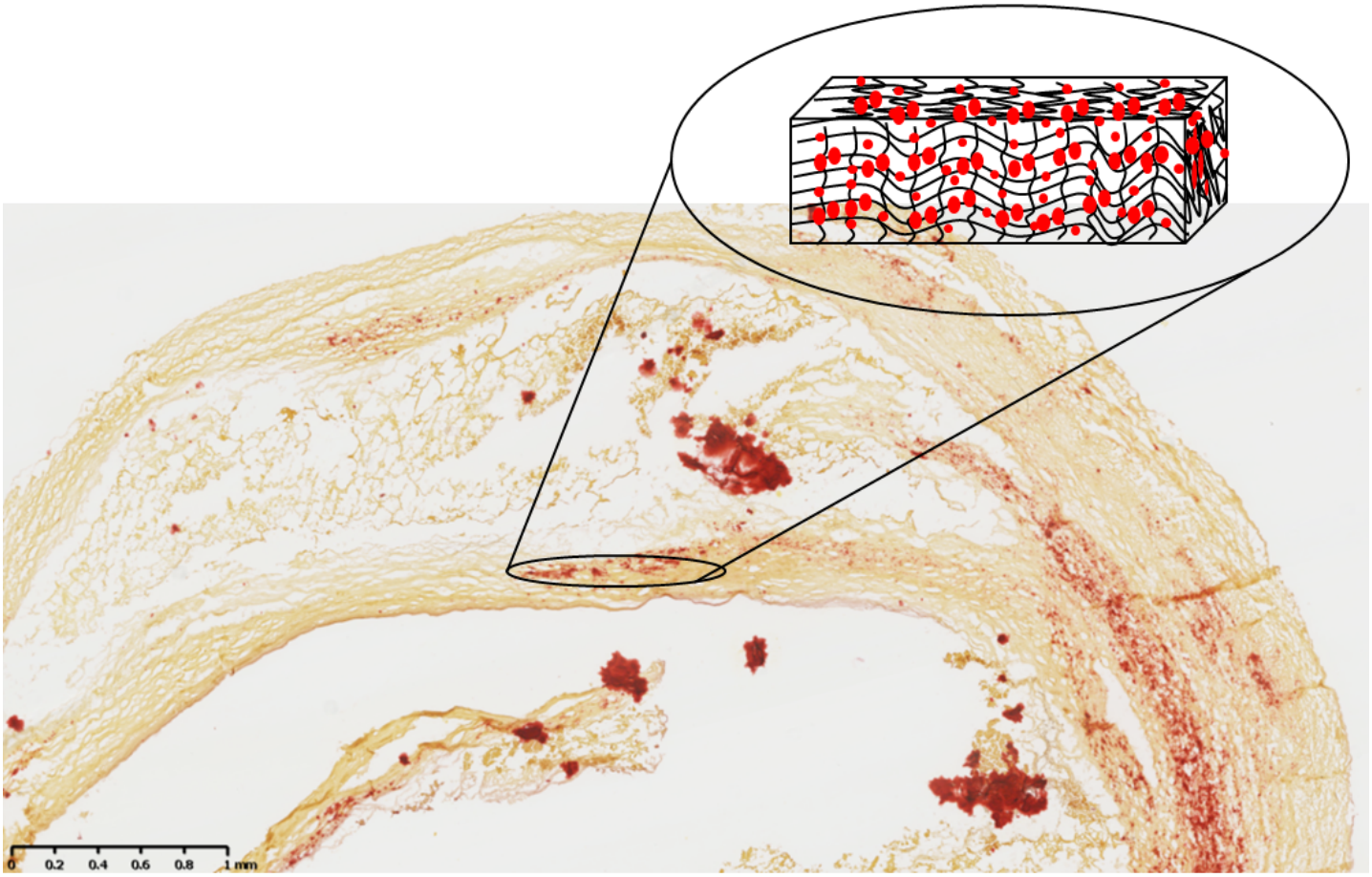

TU Delft Delft University of Technology

Erasmus MC
Universitair Medisch Centrum Rotterdam

Mechanical and Structural Characterisation of a Calcified Scaffold

Towards the Development of an In-Vitro Model of an Atherosclerotic Fibrous Cap

by

Amal Mansoor

to obtain the degree of Master of Science

at the Delft University of Technology,

to be defended publicly on Tuesday, September 24, 2019 at 13:30.

Student number: 4737040
Supervisors: Dr. Hilary Barrett (Erasmus MC)
Dr. ir. Frank Gijsen (Erasmus MC)

Dr. ir. Lidy Fratila-Apachetei (TU Delft)
Prof. Dr. ir. Amir A. Zadpoor (TU Delft)

Acknowledgements

This project was completed with the help, encouragement and support from many people. My daily supervisor, Hilary Barrett's encouragement and patience helped guide me throughout this project. She was always ready to answer my questions and pushed me to think critically, even when I stopped her at the coffee machine with my million questions. Frank Gijsen's input during the brain storming sessions was critical in helping me view my results analytically. I am also grateful for their help in presenting my findings in a more scientific manner. I would like to thank my TU Delft supervisor, Lidy Fratila-Apachetei for her guidance and support during the project. This project would not have kicked off without the collaboration and support from the Orthopaedics department at Erasmus MC. I would like to thank Eric Farrell for working with us on this project in the first phase of creating the calcified scaffolds in his lab and setting up the cell culture study. I would especially like to thank Janneke Witte-Bouma for the cell culture experiments and her patience in explaining the basics of cell culture to me. A special thanks to Claudio Initini for making the collagen 1 scaffolds. I am also grateful to Ali Akyildiz for taking time out of his daily schedule to think out loud with me. I would also like to thank Kim van der Heiden for her support.

Last but not the least, I would particularly like to thank Kim van Gaalen for training me in histology and for her uplifting words, and Robert Beurskens for his help in setting up the mechanical experiments and calibrating the load cells for the umpteenth time. Also, Michiel Manten and Geert Springeling from the Instrumentation department for making the holders for the mechanical set up, always on a short notice. I would also like to thank Tijmen Roest for his help with the experiments and lending a ear when needed. A special thanks to Heleen van Beusekom and her lab for helping me with histology and the SEM in a timely manner. I am thankful to all my colleagues at the biomechanics lab for creating a lively environment, especially during lunch breaks which helped take my worries away momentarily.

Finally, my deepest gratitude to my friends and family who were extremely patient and supportive during the course of my thesis and master study. The help, support and encouragement from everyone gave me the strength to take on this journey and successfully complete it.

Amal Mansoor
Delft, September 2019

Abstract

Atherosclerosis is an inflammatory disease characterised by the formation of plaque in the intimal layer of the artery. The plaque is made of a lipid rich necrotic core which is covered by a collagen rich fibrous cap. If this fibrous cap ruptures, it can lead to sudden thrombotic occlusion of the artery. Rupture of the fibrous cap is linked to many factors. Recently, through high resolution imaging, microcalcifications have been found in the fibrous caps. The role of these microcalcifications in fibrous cap rupture mechanics is a debated theory. Calcifications, by virtue of their high stiffness, are predicted to increase local stresses in the less stiff surrounding collagen tissue by creating stress concentrations. This interaction between collagen and microcalcifications has not been studied extensively. Fibrous cap rupture mechanics can be studied through mechanical tests such as uniaxial tensile tests. Due to limitations in access to human plaque tissues and differences in the mechanisms of cap rupture in animal models, there is a need for an in-vitro platform to study fibrous cap rupture mechanics.

In this study, a simplified model of a fibrous cap incorporating two components, collagen and calcifications, for the development of an in-vitro model of an atherosclerotic fibrous cap was explored. High levels of calcium and phosphate have been found in microcalcifications in fibrous caps. Mesenchymal Stem Cells (MSCs) have been linked to vascular calcifications and have been found to deposit calcium phosphate in collagen scaffolds. Collagen type 1 scaffolds were seeded with MSCs to create calcium phosphate deposits with the aim of emulating an atherosclerotic fibrous cap from the collagen and calcifications aspect. The collagen scaffold constructs were mechanically tested to study the mechanical properties and effects of the calcium phosphate deposits on the mechanical behaviour. The structure and failure behaviour was studied through histology and scanning electron microscopy.

Deposits of calcium phosphate were successfully formed inside the collagen scaffold leading to a calcified scaffold. The calcified collagen scaffolds were mechanically and structurally characterised. The composition and size of the calcium phosphate deposits were in line with microcalcifications found in atherosclerotic fibrous caps. The failure was characterised by noticeable initial failures, multiple miniature failures and high stretch before the final complete failure. The calcified scaffolds can potentially serve as a baseline for the development of an in-vitro model of an atherosclerotic fibrous cap and for gaining useful insights into fibrous cap rupture mechanics.

Contents

List of Figures

List of Tables

1 Introduction

Atherosclerosis is a multifaceted, chronic, inflammatory, lipid-driven cardiovascular disease which is characterised by the formation of plaques in the intima, the innermost layer of the artery [1, 2]. The formation of plaques can lead to arterial dysfunction by hindering the blood flow through the arteries [2].

Atherosclerotic plaque formation is a complex and dynamic process that takes place in the arteries. A normal artery is made of three layers: adventitia (outermost layer), tunica media (middle layer) composed of quiescent smooth muscle cells (SMCs) and an ordered extracellular matrix (ECM), and the tunica intima (innermost) [3]. Plaque development begins with the formation of a fatty streak [4]. Plaque growth in the intima is triggered by the infiltration of blood-borne low density lipoproteins (LDL) in the vessel endothelium. The modification and accumulation of LDLs in the intima initiates an immune response. Monocytes exit the blood stream and penetrate the endothelium. They differentiate into macrophages, consume the LDLs and turn into foam cells. Other immune cells such as T lymphocytes also enter the intima and adjust the functions of endothelial and smooth muscle cells. Due to the death of the lipid-laden macrophages by the formation of foam cells, cellular debris and extracellular lipid droplets accumulate to form a fatty streak [2]. The plaque development progresses into a more advanced, complex structure. Foam cells, extracellular lipid droplets and cell debris continue to accumulate to form a core region in the centre of a plaque [4]. Resident SMCs from the intima and recruited SMCs migrate from the media into the intima, and produce ECM molecules such as interstitial collagen and elastin. This contributes to the thickening of the intima, leading to the formation of a fibrous cap [3]. A fibrous cap is a structure of varying thickness, made of a dense collagen-rich extracellular matrix with cells such as vascular smooth muscle cells, macrophages and T cells (immune cells) overlying the lipid-rich necrotic core [4, 5].

The formation of plaques is also accompanied by vascular calcification. Calcification can form in the fibrous cap and necrotic core [6]. Vascular calcifications have multiple origins such as the differentiated intimal cells (apoptotic vascular SMCs or macrophages and their matrix vesicles (MVs)) or undifferentiated progenitor cells, either resident within the vessel wall or from the circulation [7, 8]. MVs have been looked into extensively as a critical source for calcification initiation and progression. Recently, progenitor cell populations such as mesenchymal stem cells (MSCs) have been found to have an intrinsic capacity for vascular calcification in an atherosclerotic environment. Due to their multi-potency, these cells can differentiate to form calcifications in a vascular environment [9]. Although the knowledge of resident stem progenitor populations is still at its genesis stage, they are emerging as an important player in atherogenesis and vascular calcifications [10].

1.1. Motivation

If the pro-thrombotic material (necrotic core) in the plaque is exposed to the blood, it can lead to sudden thrombotic occlusion of the artery. This can lead to myocardial infarctions in the heart or ischaemic strokes in the brain [4]. This thrombosis can be caused by fibrous cap ruptures (55-65%), cap erosions (30-35%) and calcified nodules (2-7%), leading to sudden coronary deaths [11]. Fibrous cap ruptures can be caused by many factors. An illustration of a ruptured fibrous cap is shown in Figure 1.1. It is of great clinical interest to find these factors and stabilise the fibrous cap. The susceptibility of the fibrous cap to rupture increases, when its structural stability provided by the collagen, is lost. This can happen when the ability of SMCs to synthesise collagen is compromised by cell mediators or when the collagen is degraded by matrix metalloproteinases (MMPs) produced by activated macrophages. This leads to thinning of the fibrous cap [3].

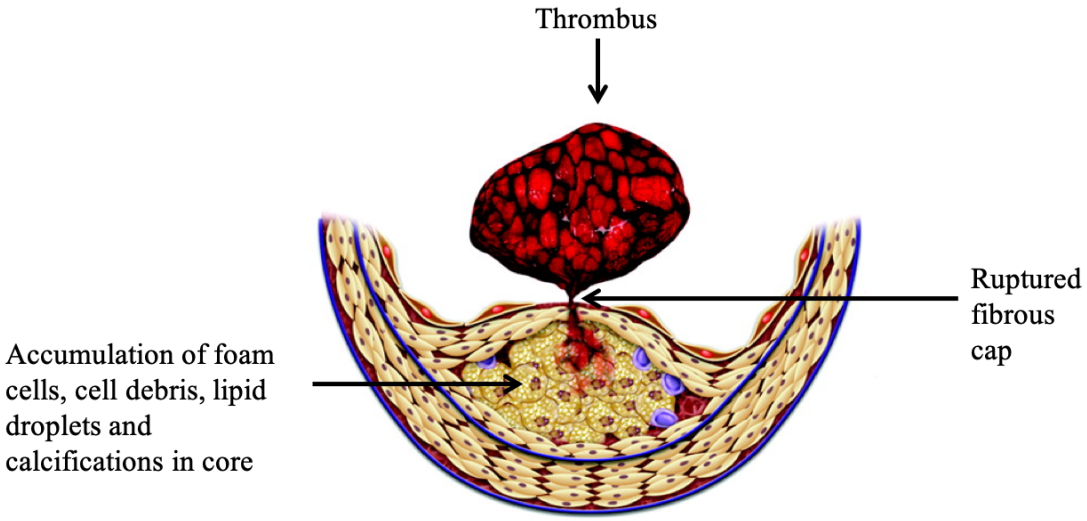

Figure 1.1: Illustration of a ruptured fibrous cap in a plaque: Rupture of fibrous cap leading to exposure of the accumulated mass in the core and subsequent thrombus formation. Adapted from Libby et al. [12]

Another cause of fibrous cap instability is due to the calcifications. The role of calcifications in fibrous cap rupture is a debated theory. Calcifications, depending on their shape, size and location in plaques have been linked to fibrous cap rupture. Microcalcifications of sizes < 50 μm have been found in fibrous caps [13]. Microcalcifications can also form within the necrotic core [14]. Macrocalcifications are usually greater than 200 μm and are found in the core [15]. A 2.1 μm high resolution micro computed tomography (micro-CT) image of microcalcifications and macrocalcifications found in a plaque is shown in Figure 1.2. Large macrocalcifications can be seen in the core (C) and clusters of microcalcifications can be seen in the fibrous cap (FC). Through biomechanical studies, microcalcifications have been predicted to increase stresses in a fibrous cap leading to instability [13, 15–17], while macrocalcifications have been predicted to not increase stresses [18, 19]. Studies have found dissimilarities in the material properties between collagen and calcifications [20]. An inverse relationship has been found between collagen and microcalcifications suggesting that thinning of fibrous cap is accompanied by microcalcification formation [21].

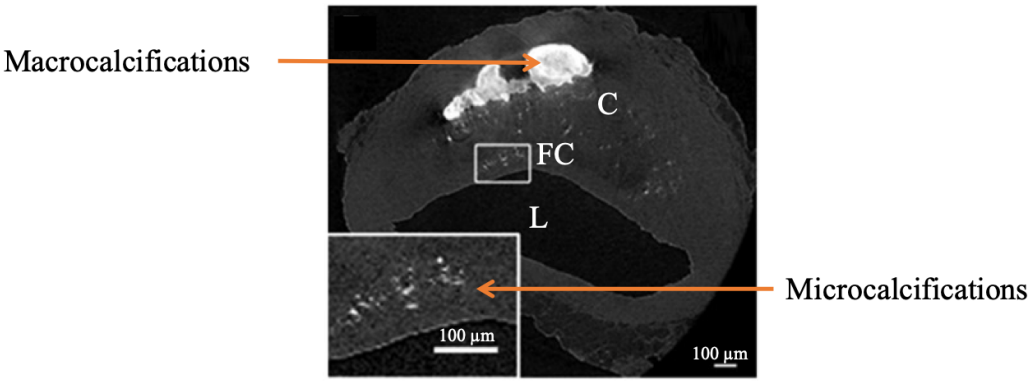

Figure 1.2: 2.1 μm high resolution micro computed tomography (micro-CT) image of microcalcifications and macrocalcifications: Clusters of microcalcifications in the fibrous cap and at higher magnification in the inset, and macrocalcifications in the core; C: Core, FC: Fibrous cap, L: Lumen. Adapted from Kelly-Arnold et al [13].

The unpredictable nature of rupture makes it difficult to study the mechanics of fibrous cap rupture in-vivo. Atherosclerosis doesn't affect many species without genetically inducing it. It only affects humans and 1 or 2 other species, such as pigs and certain primates [22]. Transgenic mice have to be genetically modified to induce atherosclerosis by knocking out the ApoE gene. These mice models do have similarities to the disease manifestations and phenotypes shown in humans. They can be used to explore certain features of the disease, such as exploring the function of particular genes or isolated features of plaques. Despite this, the underlying molecular mechanisms can differ greatly between mice and humans with the same disease phenotype [23]. They are less helpful in studying complications such as rupture and thrombosis [22].

Mechanical tests such as compression and tensile tests have been carried out on human plaque tissues ex-vivo to investigate their mechanical properties. When studying fibrous cap rupture from a mechanical view point, the cap could rupture when the external forces on the cap exceed its strength [24]. Mechanical tests can help characterise the mechanical behaviour of plaques and extract their mechanical properties. Tensile tests have been used to assess material properties sufficiently. The integration of components such as calcifications in a tissue might influence the tissue's mechanical behaviour more in a tensile test than in a compression test [25]. Although studies have carried out tensile tests on fibrous caps [24, 26, 27], the fibrous caps were not analysed for microcalcifications. Varied mechanical behaviours were observed in these studies which were not evaluated. The likelihood of a close interaction between the mechanical properties and tissue microstructure such as microcalcifications was not investigated [28]. Furthermore, to study fibrous cap rupture and these relationships, constant access to human atherosclerotic plaque is necessary. There is in some degree a limitation in access to human atherosclerotic plaques in-vivo. Systems which can be controlled in-vitro in a laboratory setting are required [29].

Hence, there is a need for a suitable platform to study fibrous cap rupture mechanics. This can potentially be solved by using tissue engineered constructs. Since a fibrous cap is composed of a dense collagen-rich extracellular matrix, collagen scaffolds can potentially be used to imitate the ECM of the fibrous cap. One of the highly-debated factors leading to fibrous cap rupture is the presence of microcalcifications. High levels of calcium and phosphate have been found in calcifications formed in plaques [30]. MSCs have been suggested to be a potential promoter of vascular calcification [9]. In-vitro, MSCs have been found to undergo osteogenic differentiation and deposit calcium phos-

phate in collagen scaffolds [31]. Hence, collagen scaffolds with these calcium phosphate deposits could be created. These collagen scaffold constructs could then be mechanically tested to investigate the effect of calcifications on the mechanical properties.

1.2. Aims of the study

The motivation behind this study was towards the development of an in-vitro model of an atherosclerotic fibrous cap to study fibrous cap rupture mechanics. The aims of this study were defined as the following:

1. Develop a collagen scaffold construct with microcalcifications: Create a calcified collagen scaffold construct to emulate a simplified model of an atherosclerotic fibrous cap with the perspective of studying collagen and microcalcifications.
2. Mechanically characterise the calcified collagen scaffold construct: Carry out mechanical tests to characterise the mechanical behaviour and failure of the collagen scaffold construct with microcalcifications.
3. Structurally characterise the calcified collagen scaffold construct: Through imaging techniques, study the morphology and failure of the calcified collagen scaffold construct.

1.3. Study outline

The study was carried out in three parts which is elaborated below:

1. Cell culture: Collagen type 1 scaffolds were seeded with paediatric-Mesenchymal stem cells to create calcium phosphate deposits.
2. Mechanical Testing: The collagen scaffolds with calcium phosphate deposits were mechanically tested by uniaxial tensile tests in comparison to collagen scaffolds without calcium phosphate deposits.
3. Histology and Scanning Electron Microscopy: The mechanically tested collagen scaffolds were studied using various stains processed by histology and scanning electron microscopy.

2

Materials and Methods

The methodology of the experiments carried out in this study are covered in this chapter. The study was conducted in three parts. In part one, collagen scaffolds were cultured with paediatric-mesenchymal stem cells (p-MSCs) to create calcium phosphate deposits. The cell culture experiments included isolation and maintenance of the cells, seeding the cells on collagen scaffolds and their subsequent osteogenic differentiation to form calcium phosphate deposits. In part two, the collagen scaffold constructs were mechanically tested by uniaxial tensile tests. Using the data from the tensile tests, Cauchy stress vs stretch ratio plots were generated and analysed. In part three, the morphologies and failure behaviours of the mechanically tested collagen scaffold constructs were studied using histology techniques and scanning electron microscopy.

2.1. Cell Culture

In this section, the methods used to prepare collagen scaffold constructs with cells to create calcium phosphate deposits are presented.

2.1.1. Collagen scaffolds

The dense extracellular matrix in a fibrous cap is made primarily of interstitial type 1 collagen. It is the major load bearing structure in the fibrous cap [32, 33]. Collagen type 1 scaffolds were used as the platform to seed cells on. Collagen scaffolds were prepared by freeze-drying 0.5% w/v collagen type I and chondroitin G Sulphate in 0.05 M acetic acid solution [SurgaColl Technologies Ltd, Dublin Ireland]. Chrondroitin G Sulphate is a type of glycosaminoglycan (GAG). GAGs help complement the biofunctionality of collagen by providing layouts for cell attachment and migration [34].

2.1.2. Cell Isolation and Maintenance

Progenitor cell populations such as mesenchymal stem cells (MSCs) have been linked to vascular calcification. An intrinsic capacity of MSCs to form calcified matrices in an atherosclerotic environment has been observed [9]. Calcium deposition by MSCs of vascular origin was also observed [35]. Elemental micro-analyses of microcalcifications in plaques have found a high amount of calcium and phosphorus [30]. Calcification progression is suggested to be initiated by the formation of small calcium phosphate rich spheres, which aggregate to form microcalcifications, and serve as the nu-

cleus for larger calcifications [8]. Due to the intrinsic capacity of MSCs to form calcifications, these cells were selected for seeding on collagen scaffolds to form calcium phosphate deposits.

For all the cell culture experiments, paediatric-mesenchymal stem cells (P-MSCs) were isolated and expanded as described by Knuth et al [36] from iliac crest biopsies of juvenile donors (ages: 9-12) undergoing cleft palate reconstruction surgery [Erasmus MC, Rotterdam: Medical Ethical Committee Number MEC-2014-106]. p-MSCs were used as they are capable of more consistent multi-lineage differentiation [36]. Cells at passage 3-4 were used in the generation of the collagen scaffold construct.

p-MSCs were first seeded at a density of 50,000 cells/cm^2 in an expansion medium (α-MEM [Life Technologies, Thermo Fisher Scientific Inc., USA], supplemented with 10% v/v heat inactivated fetal calf serum (FCS) [Invitrogen, lot 41Q2047K, Thermo Fisher Scientific Inc., USA], 1 ng/ml fibroblast growth factor (FGF2) [Bio-Rad Laboratories Inc., USA], 0.1 mM ascorbic acid-2-phosphate [Sigma-Aldrich, USA], 1.5 μg/ml AmphotericinB [Life Technologies, Thermo Fisher Scientific Inc., USA] and 50 μg/ml gentamicin [Life Technologies, Thermo Fisher Scientific Inc., USA]). After 24 hours, non-adherent cells were washed out with 2% v/v heat inactivated FCS in phosphate buffer solution (PBS) [Life Technologies, Thermo Fisher Scientific Inc., USA] and adherent cells were expanded again in the expansion medium. The expansion medium was renewed twice a week until the cells reached 80-90% confluency. Confluency refers to the percentage of a surface covered with adherent cells. In Figure 2.1, the cells in Figure 2.1(a) have been expanded for 3 days and the cells in Figure 2.1(b) have been expanded for 4 days. The cells in Figure 2.1(b) have covered a higher percentage of the surface than the cells in Figure 2.1(a) over the span of 1 day. The cells in Figure 2.1(b) have reached 80-90% confluency. Once this confluency is observed, cells were washed with PBS and dislodged with trypsin-EDTA solution [Life Technologies,Thermo Fisher Scientific Inc., USA]. These cells were then sub cultured at 2300 cells/cm^2 in the expansion medium. The expansion medium was renewed biweekly until the cells reached 80-90% confluency again [36]. All cells were cultured in a humidified atmosphere at 37^{o}C and 5% CO_2. Once the desired confluency was reached, the cells were seeded on the scaffolds.

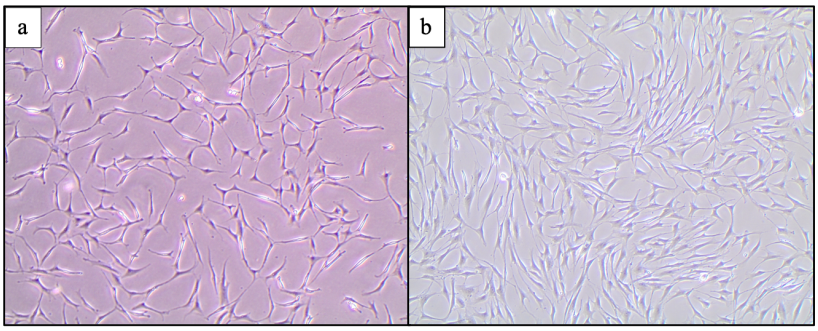

Figure 2.1: Comparison of low and high confluency: a) Low confluency observed after 3 days of cell expansion b) High confluency of 80-90% observed after 4 days of cell expansion.

2.1.3. Cell Seeding

To evaluate the optimal cell seeding approach on the scaffold, three different methods were employed. A cell suspension in α-MEM medium with 1 ng/ml FGF2 and 0.1 mM ascorbic acid-2-phosphate was seeded on the scaffold by the following three methods:

1. Passive seeding: A cell suspension of 0.25 ml consisting of 1 million cells was seeded directly

on a dry collagen scaffold that was placed on an agarose layer 2% w/v in saline (0.9% w/v) in a 6 well culture plate. The seeded scaffolds were incubated for 30 minutes at 37^{o}C and 5% CO_2 in a humidified atmosphere. After 30 minutes, the scaffolds were flipped and the other side was seeded with 1 million cells in 0.25 ml α-MEM.

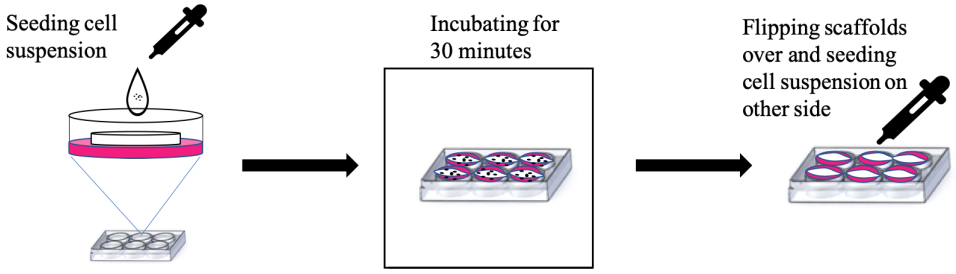

2. Semi-passive seeding: A cell suspension of 0.5 ml consisting of 2 million cells in α-MEM was seeded on a dry collagen scaffold placed in a 50 ml falcon polypropylene tube. The seeded scaffolds were incubated for 30 minutes at 37^{o}C and 5% CO_2 in a humidified atmosphere. During those 30 minutes, the tube was tapped gently 3 times every 10 minutes.

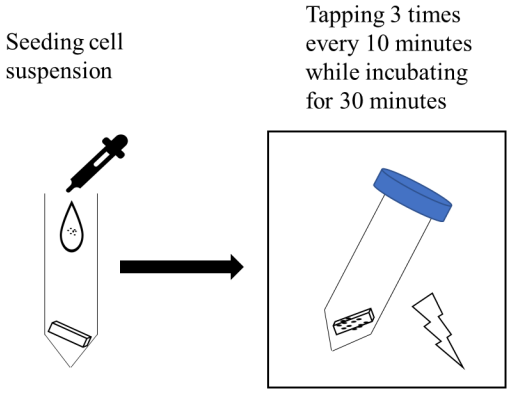

3. Dynamic seeding: A cell suspension of 0.5 ml consisting of 2 million cells was seeded on a dry collagen scaffold placed in a 50 ml falcon polypropylene tube under continuous agitation (≈70-90 rpm) while incubating for 30 minutes at 37^{o}C and 5% CO_2 in a humidified atmosphere.

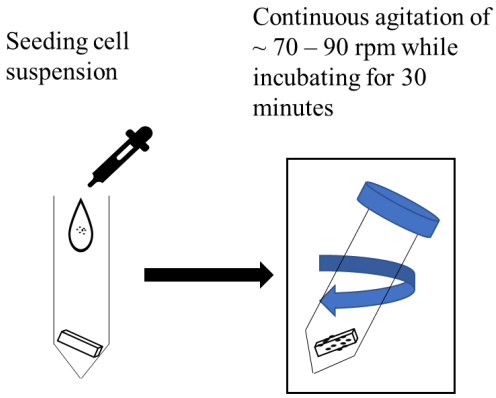

The seeded scaffolds were submerged in 4 ml final volume of α-MEM supplemented with 1 ng/ml FGF2 and 0.1 mM ascorbic acid-2-phosphate. The scaffolds were incubated at 37^oC and 5% CO_2 in a humidified atmosphere for twenty four hours. After twenty four hours, the semi-passively and dynamically seeded scaffolds were transferred to 6 well culture plates coated with an agarose layer 2% w/v in saline (0.9% w/v), while the passively seeded scaffolds remained in their 6 well culture plate. The agarose layer was used to prevent the cells from adhering to the plastic of the well plate.

2.1.4. Osteogenic Differentiation

Twenty four hours after seeding cells, expansion medium was replaced with complete osteogenic medium (DMEM high glucose [Life Technologies, Thermo Fisher Scientific Inc., USA] with 10% v/v heat inactivated FCS, 1.5 μg/mL Amphotericin B, 50 μg/mL gentamicin, 10 mM β-glycerophosphate [Sigma-Aldrich, USA], and 0.1 μM dexamethasone [Sigma-Aldrich, USA]). In-vitro, MSCs in osteogenic differentiation medium undergo osteogenic differentiation towards an osteogenic phenotype. p-MSCs are capable of this multi-lineage differentiation to osteogenically differentiated p-MSCs [36].

p-MSC's have an intrinsic osteogenic differentiation capacity to deposit calcium phosphate. To monitor this osteogenic differentiation capacity, the same p-MSC's seeded on the scaffolds, were seeded to form a monolayer. A monolayer is a cell culture of a single layer of cells. They were seeded at 3000 cells/cm^2 in expansion medium. After twenty four hours, the medium was replaced with the complete osteogenic differentiation medium. These cells expand to form a monolayer which starts to deposit calcium phosphate. This helps monitor calcium phosphate deposition. If the monolayer managed to create deposits, the cells seeded on the scaffolds should exhibit the same differentiation capacity. The osteogenic mediums of the scaffolds and monolayer were refreshed twice a week.

2.1.5. Calcium Assay

To monitor the calcium phosphate formation, a reverse assessment was carried out. A drop in the calcium levels in the culture medium indicated an uptake of calcium and hence potential formation of calcium phosphate deposits by the cells. The assay is based on the reaction of calcium with o-cresophthalein complexone in an alkaline solution. A colour change from light brown-greyish (light taupe) to a bright purple-coloured complex indicates the formation of Ca^{2+}-o-cresolphthalein complex. The intensity of the pink-purple colour is proportional to the calcium concentration in the sample. $CaCl_2$ ranging from 0-3 mM in calcium free α-MEM was used to determine the Ca^{2+} content in the cell culture supernatants (medium whose calcium has to be measured). In this study, the cell culture supernatants were the mediums from the scaffolds and monolayers. An osteogenic differentiation medium with no cells was also included as a control.

2.2. Mechanical Testing

Two types of collagen scaffold constructs were tested. Sixteen calcified scaffolds (prepared through cell culture) and six collagen scaffolds without any cells were tested. The collagen scaffolds without cells, hence no calcium phosphate deposits, are referred to as non-calcified scaffolds from here on. The dry non-calcified scaffolds were immersed in PBS prior to testing. The original size of the calcified scaffolds before cell seeding was 15 x 10 mm (length x width). Due to cell seeding, the calcified scaffolds shrank to lengths ranging from 5.48 to 9.65 mm and widths ranging from 3.37 to 7.76 mm. The average size was 7.26 x 4.65 mm (length x width). The non-calcified scaffolds were tested at dimensions close to that of the calcified scaffolds. The lengths and widths of the non-

calcified scaffolds ranged from 6.978 to 9.907 mm and 5.291 to 6.652 mm, respectively. The thickness of the scaffold was measured on an empty scaffold, first immersed in PBS, to be approximately 1.2 mm. This thickness measurement was assumed for all calcified and non-calcified scaffolds. Any shrinkage in the thickness of the calcified scaffolds was assumed to be negligible.

2.2.1. Experimental setup

An in-house designed tester, consisting of a linear actuator [Oriental Motor Ltd., Japan], 10 N load cell [Omega Engineering Inc., USA] and a digital multimeter [Siglent (SDM3045X) Technologies Co., Ltd., China] was used to perform the uniaxial tensile tests. The experimental set-up is presented in Figure 2.2. Two clamps were used to secure the scaffold in place: A stationary clamp attached to the load cell and a moving clamp attached to the actuator. Foam tape covered with sandpaper was stuck to the clamp surfaces to prevent slippage of the scaffold during loading. The tests were carried out at 37^{o}C to mimic body temperature and keep the scaffolds hydrated during testing. To attain this temperature and hydration, the clamps were placed in a PBS bath with a heating element. A digital microscope camera [Carl Zeiss Microscopy GMBH, Germany] attached to a lens tube mounted above the tensile tester was used to capture an image every second. Two adjustable light sources were used to attain the right lighting to acquire clear images.

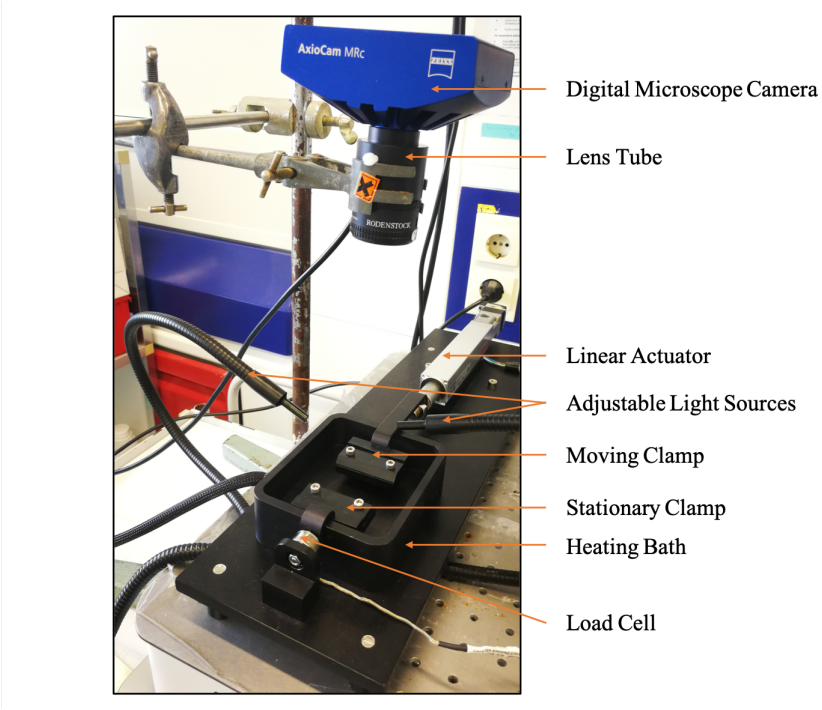

Figure 2.2: In-house designed uniaxial tension tester with the different components pointed out.

The scaffold was clamped in place, keeping a distance of 2 mm between the clamps. The scaffold was then pre-loaded by pre-stretching to 0.5 mm resulting in a final gauge length of 2.5 mm. Due to the small dimensions of the scaffold, the pre-load was fixed by always stretching to 0.5 mm to prevent over-stretching of the scaffold before the pre-conditioning. Five pre-conditioning cycles were carried out at a speed of 0.03 mm/s to an extension of 0.5 mm. After five pre-conditioning cycles, the scaffold was pulled at a speed of 0.03 mm/s. The speed was chosen based on the dimensions to maintain quasi-static testing conditions. The tests were performed until the scaffolds were pulled apart sufficiently but not separated completely. One calcified scaffold was tested until the scaffold

separated into two pieces to study the rupture surfaces from the cross section.

Stretch ratio (λ) and Cauchy stress (σ) were calculated from the displacement and force values using equations 2.1 and 2.2 respectively.

$$\lambda = \frac{L}{L_o} \tag{2.1}$$

$$\sigma = \lambda \frac{F}{A_o} \tag{2.2}$$

L_o is the initial gauge length, L is the instantaneous length during stretching, F is the force recorded during the test and A_o is the initial cross sectional area at rest. To calculate A_o, the thickness and width at rest were used. Mechanical properties of soft biological tissues are calculated under the assumption of incompressibility. Incompressibility means the volume of a material remains constant during deformation [37]. In this study, the stress calculations were carried out with this assumption.

2.2.2. Data Smoothing

The experimental data was smoothed using a centred moving average fit to eliminate noise. A moving average fit is widely used to filter out noise from random short-term fluctuations in data. This fit helps to smooth the original data by capturing the important trends without all the minor fluctuations [38, 39]. For the moving average, firstly a low number of sampling points based on the sampling rate of the experiment was chosen. A low sampling point moving average is more susceptible to short term noise [40]. This was observed in this study's experimental data as its sampling rate of the experiment would record noise as well. The number of sampling points was increased by trial and error till a value where the noise was sufficiently cancelled out without losing important small changes in stresses was found. Hence, the experimental data was averaged over 100 sampling points. An example of the centred moving average fit carried out on the original experimental data is shown in Figure 2.3. The original experimental data is shown in Figure 2.3(a) and the centred moving average fit is shown in Figure 2.3(b). The small change in slope in Figure 2.3(a), pointed out by the black arrow, is preserved in Figure 2.3(b) after smoothing. All calculations were carried out on the filtered data.

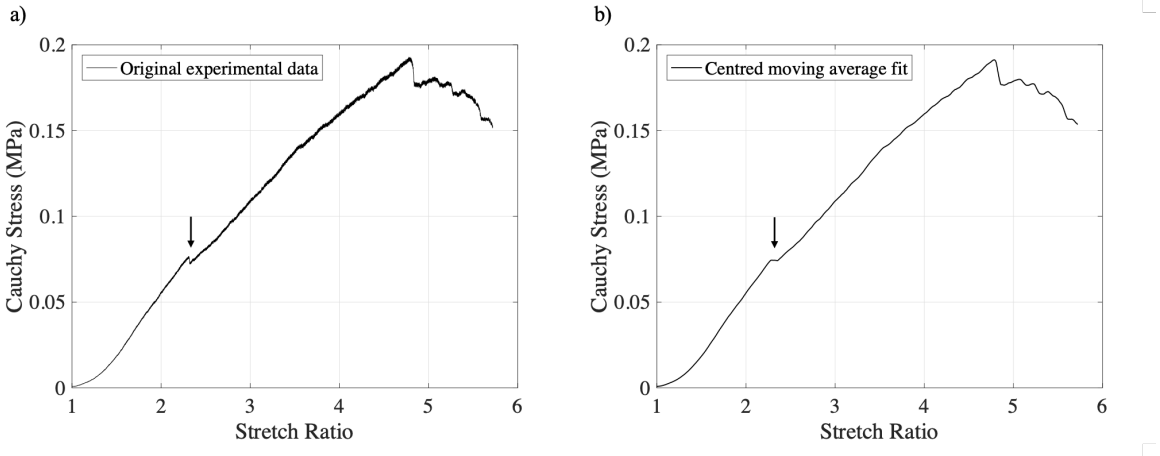

Figure 2.3: Cauchy stress vs. stretch ratio plots of a) Original experimental data with no smoothing, b) Centred moving average fit; Black arrows indicate a change in slope in the original data preserved after smoothing.

2.2.3. Rupture initiation

On initial visual observation of the fitted plot of Cauchy stress vs stretch ratio, a drop in the stress values was noted before the peak stress drop off in the graphs. An example of this is pointed out in Figure 2.4 by the black solid arrow. To ensure that this drop in stress value corresponds to a rupture, recorded images of each experiment were analysed on GOM correlate software [GOM GmbH, Germany]. Each image was inspected carefully to find the first identifiable tear. Once an identifiable tear was found, the gauge length in the image was measured. At the same gauge length in the stress vs stretch plots, the plots were inspected to verify if the first identifiable tear refers to the first drop in stress. Out of the 16 calcified scaffolds tested, the first identifiable tear was the same as the first drop in stress in 7 scaffolds. Out of the 6 non-calcified scaffolds, the first identifiable tear was the same as the first drop in stress in 5 scaffolds. Rupture points in the other graphs could not be observed visually since the images taken by the camera only capture the surface of the scaffold. Ruptures that take place inside the scaffold or out of view for the camera were not recorded. This change in stress value is defined as an initial rupture point in this study. To detect these initial rupture points in each experimental data without bias or interference from noise recorded during testing, the slope of the curve was calculated. To remove the interference of noise, a centred moving average fit was carried out on the slope values. A plot of the slope values calculated over the fitted experimental data is presented in Figure 2.4.

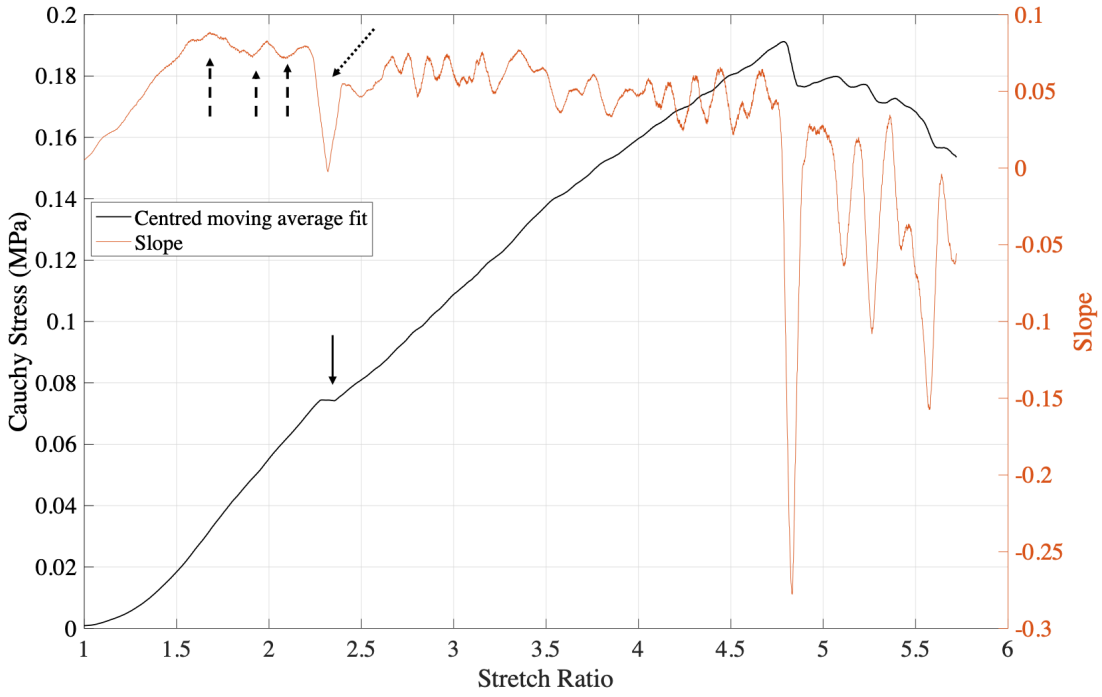

Figure 2.4: Cauchy stress vs stretch ratio plots of fitted experimental curve in black and fitted slope in orange; The black solid arrow indicates a drop in stress before the peak stress drop off, the black dashed arrows indicate micro-failures and the black dotted arrow indicates an initial rupture point.

As seen in Figure 2.4, there are multiple slope changes before the peak stress drop off which can be considered as initial ruptures. To find the change in slope that corresponds to a macroscopic initial failure, a slope change value was chosen. To choose this value, the difference between the value of the slope at the point where the slope starts decreasing and the value of the slope where it

starts to increase again was calculated in the seven out of sixteen calcified scaffolds, where the first identifiable tear was a drop in the stress value. This difference was calculated to be approximately 0.02 in the seven scaffolds. This value was used as a threshold. Keeping this value in mind, each plot of slope-stretch ratio and stress-stretch ratio was inspected. The first difference in slope whose value was greater than or equal to 0.02 was considered as an initial rupture. An example of this is shown in Figure 2.4, pointed out by the black dotted arrow. Any changes in slope before this with a slope difference value less than 0.02, was considered as a failure not visible macroscopically. Examples of these are shown in Figure 2.4, pointed out by the black dashed arrows. These changes in slope before the defined initial rupture point were not visible in the fitted experimental curve. Even after smoothing the slope curve, these smaller changes in slope were preserved due to the sensitivity of the load cell. These failures are defined as micro-failures. Hence using the slope differences, the stresses and stretch ratios at the initial rupture points were extracted from the fitted experimental data. The MATLAB code is included in the Appendix A.1.

2.2.4. Ultimate Tensile Strength (UTS)

To be consistent with literature, ultimate tensile strength (UTS) values were recorded as well. This is defined as the maximum resistance a tissue has to fracture. It is equivalent to the maximum load that the cross-sectional area can carry when a load is applied [27]. It is the point of failure beyond which an increase in stress is not observed on further stretching [41]. In this study, UTS is referred to as final failure. The stresses and stretch ratios at these final failure points for each scaffold were recorded.

2.2.5. Averaging

The mechanical behaviour of the calcified collagen scaffold constructs was compared to studies that tested fibrous caps. The study by Teng et al [24] tested fibrous caps. To follow the same methodology for accurate comparison among all studies, the averaging method employed by Teng et al [24] was used to generate the average curve for this study and other studies that tested fibrous caps. The Cauchy stress-stretch ratio data were digitised from the studies. Each experimental data in this study and other studies was averaged in order to represent the mechanical behaviour with one representative curve respectively. The stresses and stretch ratios were averaged in small energy intervals separately. The elastic energy at each stretch interval was calculated by the equation 2.3. For each scaffold, 100 equal intervals were placed between the maximum and minimum strain energy. At each interval, the stresses and stretch ratios were averaged among all the test data for each study. The MATLAB code is included in the Appendix A.2.

$$W(\lambda) = \int_1^{\lambda} \sigma(\lambda) d\lambda \tag{2.3}$$

where W is the strain energy density, λ is the stretch ratio and σ is the Cauchy stress.

2.2.6. Tangential Moduli

To calculate the tangential modulus, the stretch-stress relationship of each scaffold was characterised using a modified Mooney-Rivlin strain energy density function. Mooney-Rivlin functions are used to characterise non-linear elasticity, hyperelasticity, by relating the stretch ratios and stresses

through a strain energy density function as shown in equation 2.4.

$$W = c_1(I_1 - 3) + D_1[e^{D_2(I_1-3)} - 1] + K(J-1) \tag{2.4}$$

where I_1 and J are the first invariant and Jacobian of the deformation gradient tensor, respectively, D_1 and D_2 are the material constants and K is Lagrange multiplier for incompressibility. Since incompressibility is assumed for the scaffolds, $J = 1$.

The derived stress equation is shown in equation 2.5. The derivation of the equation is included in the Appendix A.3.

$$\sigma = 2c_1(\lambda^2 - \frac{1}{\lambda}) + 2D_1D_2e^{D_2(\lambda^2+\frac{2}{\lambda}-3)(\lambda^2-\frac{1}{\lambda})} \tag{2.5}$$

Each experimental data was fit to σ using the curve fitting toolbox on MATLAB [2017b MathWorks, Massachusetts, USA] to obtain the material constants. The materials constants c_1, D_1 and D_2 were constrained at the lower bound to zero. To calculate the tangential moduli, equation 2.5 was differentiated with respect to the stretch ratio (λ). Material constants of each scaffold was inserted in the derivative of equation 2.5 to calculate tangential moduli at initial rupture points. This was done separately for the calcified and non-calcified scaffolds. The MATLAB code is included in the Appendix A.4.

2.3. Histology

2.3.1. Fixation and Processing

Each mechanically tested scaffolds was placed in a cassette and fixed in 3-4% formalin. An example of a scaffold placed in a cassette is shown in Figure 2.5(a). After 48 hours of fixation, the scaffolds were moved to PBS and refrigerated. Fixation is necessary to prevent tissue autolysis and putrefaction [42]. Following fixation, the scaffolds were processed. Processing involved three steps. The first step was dehydration using alcohol to remove water and formalin from the tissue. The second step was clearing using an organic solvent, xylene to remove alcohol and allow infiltration of paraffin wax, the embedding agent. In the final step, the scaffolds were infiltrated with paraffin wax [42]. Following this, each paraffin infiltrated scaffold was taken out of the cassette and embedded in a block of molten paraffin wax. A representation of a scaffold embedded in a paraffin block is shown in Figure 2.5(b). The paraffin wax acts as a support matrix for the scaffold while sectioning [42]. The thickness, length and width are marked to draw attention to the orientation of the scaffold in the paraffin block. T marks the thickness of the scaffold into the paraffin block.

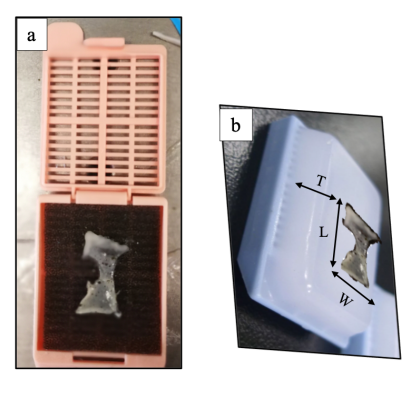

Figure 2.5: (a) Mechanically tested scaffold placed on a cassette before fixing in 3-4% formalin, (b) Representation of the scaffold embedded in the paraffin block.

2.3.2. Sectioning

The scaffold embedded in the paraffin block was cut into sections to place on slides for staining. Before sectioning, the block was chilled on an ice tray. The block was sectioned on a microtome at a thickness of 5 μm. The cut ribbons were transferred to a warm water bath to stretch the sections and prevent wrinkles. The warmed cut sections were placed on charged glass slides and placed in the incubator for a minimum of 48 hours.

2.3.3. Staining

The cut sections on the slides were stained to visualise different components in the scaffolds. Three different stains, Haematoxylin-Eosin, Miller's Elastin and Von Kossa, were used to visualise cells, collagen fibres and calcium deposits respectively. For all the stains, the slides were de-paraffinised to distilled water and then stained with the corresponding stains. Following each staining process, the slides were cleared in xylene and a cover slip was placed over the slide using Entellan (synthetic mounting medium).

Haematoxylin-Eosin staining
H&E stain was used to visualise the distribution of cells in the scaffold. The nuclei of cells stain purple. It also stains the collagen fibres pink. Haematoxylin [Klinipath B.V., Netherlands] and Eosin [Klinipath B.V., Netherlands] were used for staining.

Miller's Elastin staining
Miller's Elastin stain was used to visualise the collagen fibres. Collagen fibres stain purple. It also stains nuclei of cells brown. Slides were de-paraffinised to distilled water. Miller's Elastin [Clin-Tech Ltd, UK] and Van Gieson [Clin-Tech Ltd, UK] were used for staining.

Von Kossa staining
Von Kossa stain was used to visualise the calcium phosphate deposits formed in the scaffold. The phosphate component in calcium phosphate deposits stains black/brown. The cells can be visualised as blue using the counter-stain Thionin. Silver nitrate solution [Sigma-Aldrich, USA] was used for staining.

Images of the stained slides were taken on the Nanozoomer scanner [Hamamatsu, Japan]. The scanned images were analysed on the NDP.view2 software [Hamamatsu, Japan]. Quantification of calcium phosphate deposits were carried out on ImageJ and BioPix software. The size of the calcium phosphate deposits was calculated on ImageJ. Since the deposits were irregular in shape, the deposits were assumed to be circular to calculate the diameter [43]. To quantify the amount of calcium phosphate deposits in each calcified scaffold, images of the Von Kossa stain were exported from NDP.view2 at a resolution of 2.5x. On BioPix, an area of interest which excluded the regions of the scaffolds under the clamps were marked. The colours corresponding to the calcium phosphate deposits were selected. These results were exported as ratios of area of calcium phosphate deposit to area of selected region.

2.4. Scanning electron microscopy (SEM)

Images were taken on the scanning electron microscope (SEM) [JEOL JSM 6610LV, Japan] to observe the ruptured collagen fibres and calcium phosphate deposits. The energy dispersive x-ray spectroscopy (EDX) attachment on the SEM was used to detect the calcium and phosphate composition in the deposits. The scaffolds were fixed in 4% paraformaldehyde for at least 48 hours. After 48 hours of fixation, the scaffolds were moved to 0.1 M cacodylate buffer. The scaffolds were dehydrated with gradients of alcohol concentrations and dried overnight in Hexamethyldisilazane (HMDS). Before imaging, the scaffolds were sputter coated with a thin gold layer to improve electrical conductivity. Images were taken from the surface and cross section at a working distance of 12 mm and acceleration voltage of 10 kV.

2.5. Statistical Analysis

All statistical data were generated using SPSS statistical software [SPSS 20 Inc., Chicago, IL, USA]. A p value < 0.05 was defined as statistically significant in this study. At first, all data sets were assessed for normality using the Shapiro-Wilk test. Shapiro Wilk test was used as it is more appropriate for small sample sizes. If the significant value was greater than 0.05, the data was normally distributed. For a normally distributed data set, an independent samples t test was used. If the significance value from Levene's test for Equality of Variance was greater than 0.05, the significant value of a 2 tailed test was considered. If the significant value from the Shapiro-Wilk test was less than 0.05, the data was not normally distributed. For a data set not normally distributed, a non parametric test of 2 independent samples test was used. Under the 2 independent samples test, the Mann-Whitney U test type was used. The significant value of the 2 tailed test was considered. Statistical analysis was carried out between calcified and non-calcified scaffolds.

3

Results

3.1. Cell Culture

In this section, the results of culturing collagen scaffolds with paediatric mesenchymal stem cells (p-MSCs) to create calcium phosphate deposits are presented. Three seeding methods, passive, semi-passive and dynamic, were explored to find the optimal cell seeding method for cell migration into the scaffolds. Collagen scaffolds were seeded with cells using the optimal seeding method for mechanical tests.

Two scaffolds each, were seeded with cells by the passive, semi-passive and dynamic methods as explained in section 2.1.3. Cells were also seeded to form six monolayers as explained in section 2.1.4. Four osteogenic differentiation mediums with no cells were included as controls. The cell culture setup is illustrated in Figure 3.1. The scaffolds and monolayers were cultured for two day points (7 & 24) to monitor the changes from early in the culture to later on in the culture. To detect the cells and calcium phosphate in the scaffolds and monolayers, two types of stains, H&E and Von Kossa, were used respectively. Calcium levels in the mediums for the calcium assay were also measured at each day point.

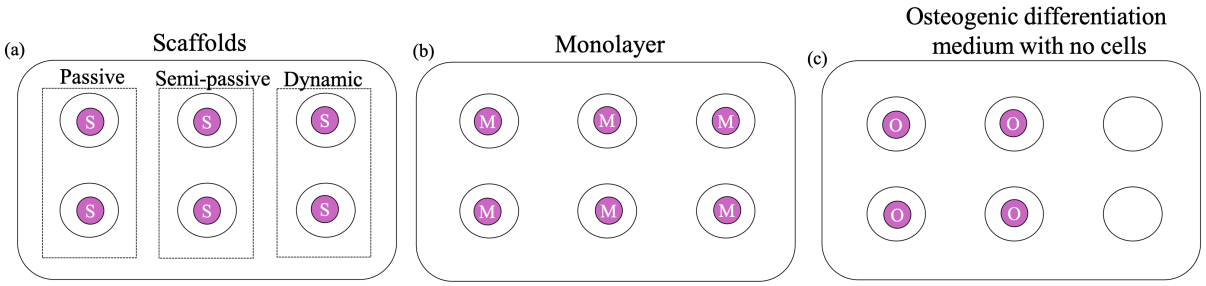

Figure 3.1: Illustration of the scaffolds seeded by each method, monolayers and osteogenic differentiation mediums with no cells: a) 2 scaffolds each seeded by the passive, semi-passive and dynamic methods, b) 6 monolayers (c) 4 osteogenic differentiation mediums with no cells.

A Von Kossa stain of a monolayer on day 7 is presented in Figure 3.2. The Von Kossa stain was positive for calcium phosphate deposits. Black calcium phosphate deposits, indicated by orange

arrows, can be seen in the Figure 3.2. The deposition of calcium phosphate on the monolayers indicated that the cells had an inherent osteogenic differentiation capacity to deposit calcium phosphate. This meant that the cells in the scaffold should also exhibit similar osteogenic differentiation capacities.

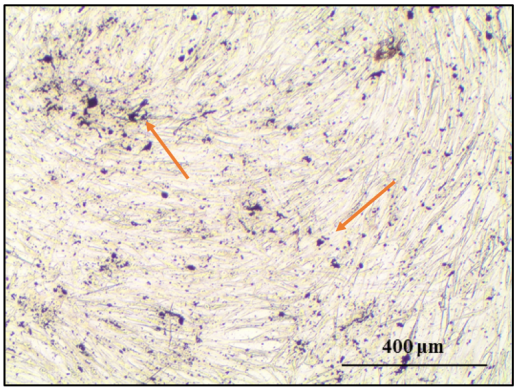

Figure 3.2: Von Kossa stain of a monolayer on day 7: Black calcium phosphate deposits were seen scattered around the monolayer, orange arrows point to the deposits.

In Figure 3.3, the H&E stains of the scaffolds cultured till day 7 are presented. The cells stain purple and the collagen fibres stain pink. No cells were seen in the passively seeded scaffolds (a & d). Cells were seen distributed in the semi-passively (b & e) and dynamically seeded scaffolds (c & f). Clusters of cells, as indicated by the black dashed arrow in Figure 3.3(e) and random distributions of cells, as indicated by the black solid arrows in Figure 3.3(e) & (f) were observed. The migration of cells into the semi-passively and dynamically seeded scaffolds were high in comparison to the passively seeded scaffolds. Out of the two seeding methods which successfully led to high cell distributions, the dynamically seeded scaffolds were damaged. The structural integrity of the dynamically seeded scaffold was affected. This can be seen in Figure 3.3(c), where the collagen scaffold is denser at the centre, pointed out by the black dashed arrow, and less dense at the edges, pointed out by the black solid arrow. The fibres at the edges probably broke apart during seeding.

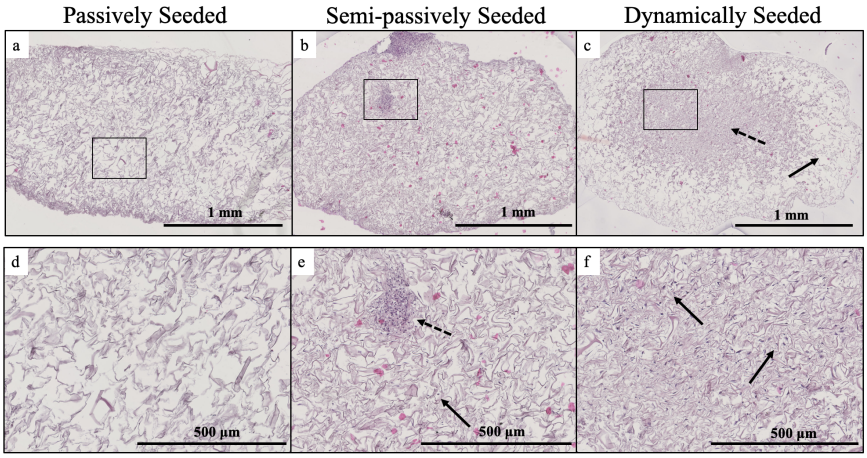

Figure 3.3: H&E stains of scaffolds cultured for 7 days using three different seeding methods: No cells were seen in the passively seeded scaffolds (a & d), Clusters, pointed out by the black dashed arrow, and randomly distributed cells, pointed out by the black solid arrows, were seen in semi-passively (b & e) and dynamically seeded scaffolds (c & f); Top row: Images taken at a low magnification, Bottom row: Images taken at a high magnification of the marked regions.

In Figure 3.4, the H&E stains of the scaffolds cultured till day 24 are presented. No cells were observed in the passively seeded scaffolds (a & d). There were no differences in the passively seeded scaffolds of day 7 and day 24. By day 24, the concentration of cells observed in the semi-passively (b & e) seeded scaffold had increased. The concentration of cells in the dynamically seeded scaffolds (c & f) had increased but looked less than the semi-passively seeded scaffolds. The structural integrity of the dynamically seeded scaffold had broken down more. The collagen scaffold was fragmented in the centre as indicated by the black arrow in Figure 3.4(c). Due to this fragmentation, the distribution of cells could not be seen clearly.

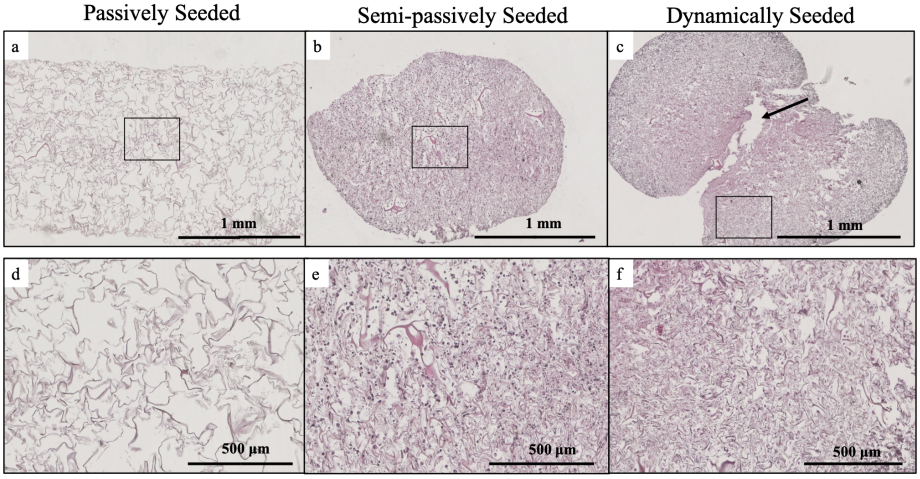

Figure 3.4: H&E stains of scaffolds cultured for 24 days using three different seeding methods: No cells were seen in the passively seeded scaffolds (a & d), Higher concentration of cells were seen in semi-passively (b & e) than the dynamically seeded scaffolds (c & f): Black arrow indicates the fragmented region of the dynamically seeded scaffold; Top row: Images taken at a low magnification, Bottom row: Images taken at a high magnification of the marked regions.

In Figure 3.5, the Von Kossa stains of the scaffolds cultured till day 24 are shown. Calcium phosphate deposits stain black/brown. The Von Kossa stain was positive for calcium phosphate deposits in the semi-passively (a & c) and dynamically seeded scaffolds (b & d). Since Von Kossa stains the calcium phosphate deposits, images of the passively seeded scaffold could not be captured as no deposits formed. Deposits of calcium phosphate were observed clearly throughout the semi-passively seeded scaffolds. This served as a confirmation of the cell migration and their subsequent deposition of calcium phosphate crystals in the semi-passively seeded scaffolds. The structural integrity of the dynamically seeded scaffold has been compromised a lot. The scaffold has separated into two pieces as seen in Figure 3.5(b). The collagen fibres have retracted from the centre to the edge leading to a higher density of fibres at the edges. Due to this and possibly longer exposure to light during the Von Kossa stain, the collagen fibres have stained brown as well. Hence, the calcium phosphate deposits cannot be seen as clearly (Figures 3.5(d)) as in the semi-passively seeded scaffolds. Since not many deposits were observed in the Von Kossa stains of the scaffolds seeded till day 7, those images aren't included.

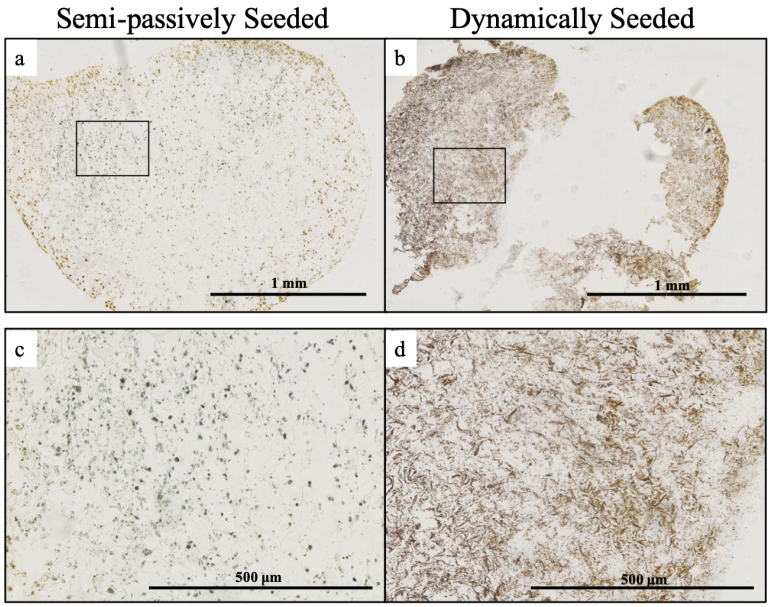

Figure 3.5: Von Kossa stains of scaffolds cultured for 24 days using two different seeding methods: Black and brown spots of calcium phosphate deposits can be seen clearly in the semi-passively (a & c) seeded scaffolds, Deposits weren't seen as clearly in the dynamically (b & d) seeded scaffolds; Top row: Images taken at a low magnification, Bottom row: Images taken at a high magnification of the marked regions.

The formation of calcium phosphate crystals in the scaffolds was further confirmed by the calcium levels measured through assays. Formation of the deposits can only be seen visually in the monolayer during culture. The formation of the deposits cannot be seen visually in the scaffolds during culture since the deposits form inside the scaffolds. Hence, to track the calcium phosphate formation in the scaffolds, calcium assays which measure the uptake of calcium by the cells were used.

In Figure 3.6, the calcium levels of the passively, semi-passively and dynamically seeded scaffolds' mediums, monolayers' mediums and control mediums from the start of culture till the end of culture (day 24) are plotted. It can be seen from the plots that the calcium levels decreased as the days progressed in the mediums of the monolayer, semi-passively and dynamically seeded scaffolds, plotted in red. The monolayers' mediums showed a decrease of 2.19. The calcium levels decreased by 2.43 and 2.37 in the semi-passive and dynamic mediums respectively. These similar decreases in calcium levels indicate that the cells migrated into the scaffolds and deposited calcium phosphate to the same extent as the cells in the monolayers did. The cells in the scaffold exhibited their osteogenic differentiation capacity. The mediums of the passively seeded scaffolds showed a decrease of only 0.59. This was in stark contrast to the decreases shown in the semi-passive and dynamic mediums. This served as an extra validation for the lack of deposits observed in the passively seeded scaffolds since no cells were seen in the scaffolds, no calcium was taken in and no deposits were formed. The control osteogenic mediums with no cells should have been constant for all the days of culture. The control osteogenic medium showed a decrease of 0.81. The control osteogenic mediums and the mediums of the passively seeded scaffolds showed a peak on day 14. This can be attributed to the sensitivity of the measurement method to its environment. Factors such as the number of times the incubator was opened causing the medium to evaporate, the number of cultures in the incubator can affect the readings. Due to this, there were some inconsistencies in the measurement readings. Since this was the only method available in the lab to monitor calcium phosphate formation in the scaffolds directly during culture, it was used as an aid to track the

formation. Barring these inaccuracies, it still provides a general impression of the decrease in Ca^{2+} concentrations and subsequently whether the cells deposited calcium phosphate.

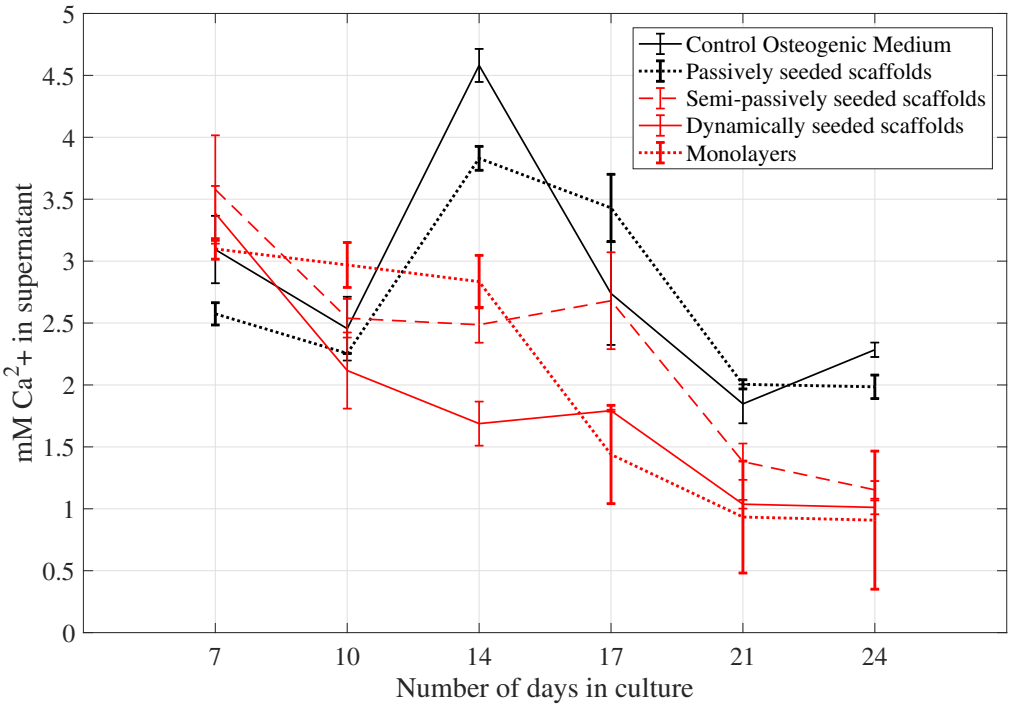

Figure 3.6: Plot of calcium levels from the start of culture till the end of culture: Monolayers (n = 6), media of the semi-passively (n = 2) and dynamically seeded scaffold (n = 2) showed the highest decrease: plotted in red, Medium of the passively seeded scaffolds (n =2) showed a negligible decrease.

Due to the high cell distributions observed and the maintenance of the scaffold's structure, the semi-passive seeding method was selected for seeding scaffolds to be tested mechanically. Four different cell donors which were comparable in osteogenic differentiation were chosen. Scaffolds were seeded with three different donors in three batches of six scaffolds for mechanical testing. Due to contaminations during culture, two scaffolds were excluded. Hence, sixteen scaffolds were mechanically tested. The fourth donor was used solely for structural characterisation. When calcium phosphate deposition was observed in the monolayers, the calcium levels in the monolayers' mediums and scaffolds' mediums were analysed for a drop in levels too. Following this, the scaffolds were kept in culture for 14 more days. By the end of the culture, the scaffolds had shrank by approximately 50%.

To summarise, cell migration into the scaffolds was attempted using three different seeding methods. Semi-passive seeding was found to be the most optimal seeding method due to high cell distributions in the scaffold without affecting the structural integrity of the scaffold.

3.2. Mechanical Testing

Uniaxial tensile tests were carried out on calcified scaffolds (n=16) prepared through cell culture and non-calcified control scaffolds (n=6) with no cells. The results of these mechanical tests are presented in this section.

An illustration of the calcified and non-calcified scaffolds before mechanically testing is shown in Figure 3.7. After seeding, the calcified scaffolds shrank by approximately 50% and decreased in porosity. The calcified scaffolds shrank from 15 x 10 mm to an average of 8 x 5 mm. The shrinkage was assumed to be negligible in the thickness. The non-calcified scaffolds were tested at the same dimensions, 8 x 5 mm. The calcified scaffolds were denser than the non-calcified scaffolds.

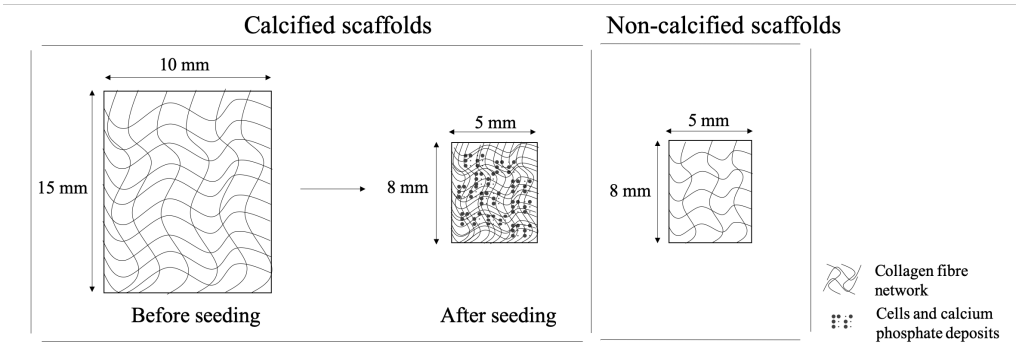

Figure 3.7: Illustration of the calcified scaffolds and non-calcified scaffolds before mechanical tests: Calcified scaffolds shrank and reduced in porosity (15 x 10 mm to 8 x 5 mm), Non-calcified scaffolds tested with the same dimensions of the calcified scaffolds (8 x 5 mm).

3.2.1. Calcified scaffolds

In Figure 3.8, Cauchy stress vs stretch ratio of all sixteen calcified scaffolds until initial rupture points are plotted. A variation in the mechanical behaviour was observed among the calcified scaffolds. The stretch ratios ranged from 1.56 to 4.50 and the stresses ranged from 0.03 MPa to 0.29 MPa. Some of the scaffolds failed at lower stretch ratios compared to the rest of the scaffolds. This variation in stretch ratios is highlighted in Figure 3.8. Three scaffolds failed at low stretch ratios less than 2, plotted in solid lines in Figure 3.8. Seven scaffolds failed at stretch ratios between 2 and 2.6 and the rest of the scaffolds failed at higher stretch ratios greater than 2.6, plotted in dotted and dashed lines respectively. Similarly, some of the scaffolds failed at low stresses, while the rest failed at higher stresses. Most of the scaffold showed a strain stiffening behaviour, with the stiffness increasing at larger stretch ratios. The values also varied among each stretch ratio group. Some scaffolds failed at stretch ratios and at higher stresses while some failed at the same stretch ratios but at lower stresses.

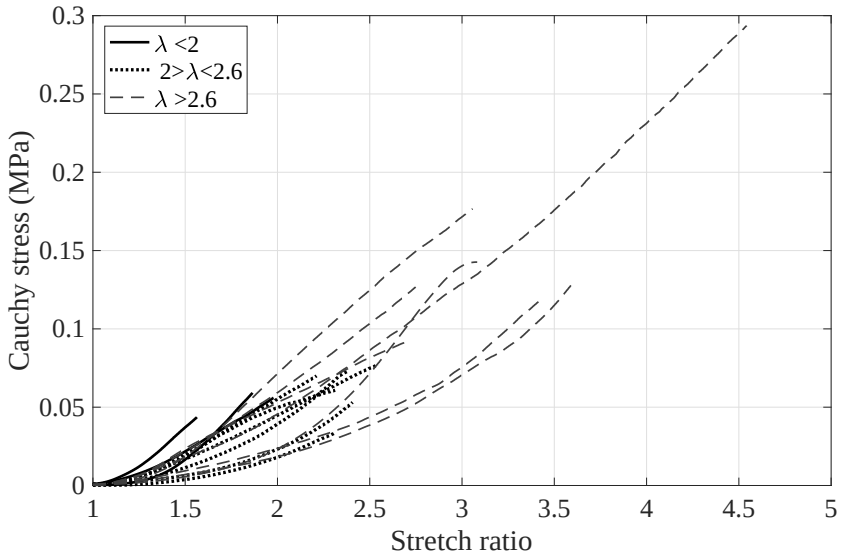

Figure 3.8: Cauchy stress vs stretch ratio plots of all sixteen calcified scaffolds until initial rupture points: Solid curves failed at stretch ratios less than 2, dotted curves failed at stretch ratios greater than 2 and less than 2.6, dashed curves failed at stretch ratio greater than 2.6; λ = Stretch ratio.

3.2.2. Non-calcified scaffolds

In Figure 3.9, Cauchy stress vs stretch ratio of all six non-calcified scaffolds until initial rupture points are plotted. The mechanical behaviour did not vary as much in the non-calcified scaffolds. The initial stretch ratios ranged only from 1.52 to 1.81. Similarly, the stress varied within a short range from 0.04 MPa to 0.15 MPa.

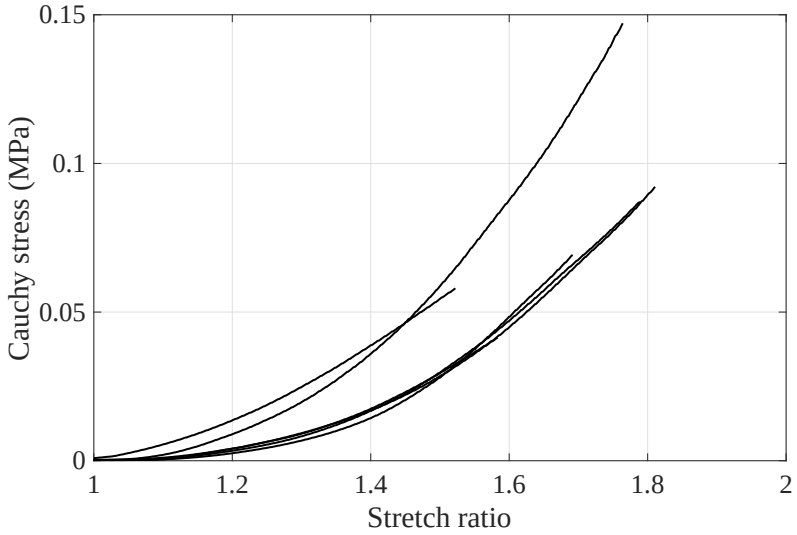

Figure 3.9: Cauchy stress vs stretch ratio plots of all six calcified scaffolds until initial rupture point.

3.2.3. Calcified vs Non-calcified scaffolds

In Figure 3.10, the Cauchy stress and stretch ratio of all sixteen calcified and all six non-calcified scaffolds are plotted until the initial rupture point. Both calcified and non-calcified scaffolds display a non-linear behaviour. On initial observation of the Figure 3.10, it was evident that the calcified collagen scaffolds reached higher stretch ratios than non-calcified scaffolds.

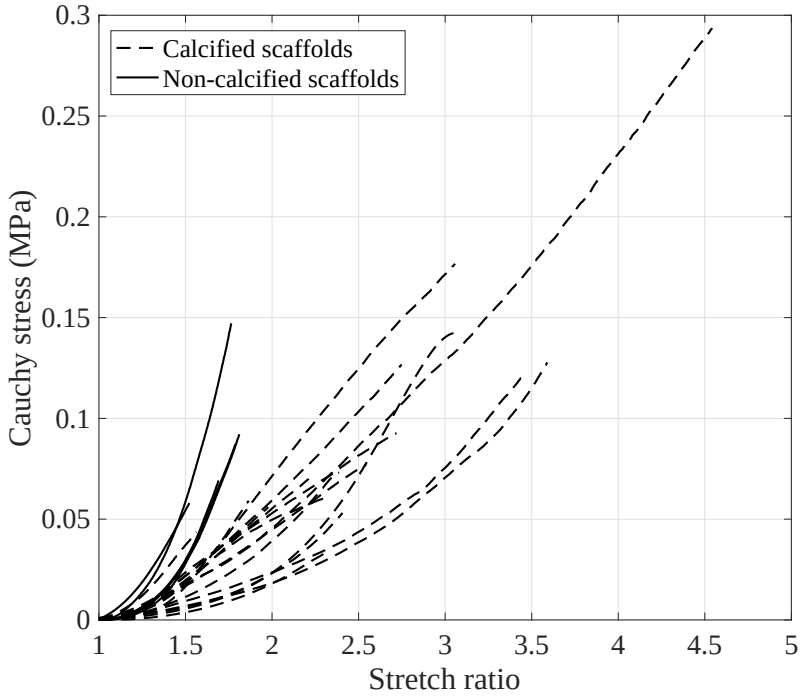

Figure 3.10: Cauchy stress vs stretch ratio plots of all the calcified (dashed curves) and all non-calcified scaffolds (solid curves) until initial rupture.

In Figures 3.11 and 3.12, the complete Cauchy stress vs stretch ratio of calcified and non-calcified scaffolds are plotted with their slopes respectively. The difference between the stretch ratios at final and initial failure points was higher in calcified scaffolds than in non-calcified scaffolds. The initial failures occurred much earlier than the final failures in the calcified scaffolds. This is pointed out in Figures 3.11 where the black dashed arrow refers to the initial failure and the black solid arrows refers to the final failure. The black dashed arrow is closer to the black solid arrow in the non-calcified scaffolds in Figure 3.12 as compared to the calcified scaffolds in Figure 3.11. Multiple failures were also observed before the initial failures and final failures in calcified scaffolds, seen as drops in the slope curve between the black dashed arrow and black solid arrow in Figure 3.11. These failures in between the initial and final failures could also be visually observed in some of the calcified scaffolds. These drops in the slope curve were not observed in the non-calcified scaffolds. In Figure 3.12, after the initial failure, the slope curve decreases linearly till the final failure. Drops before the initial failures were also seen in the slope curves of the calcified scaffolds. These were not seen in the non-calcified scaffolds.

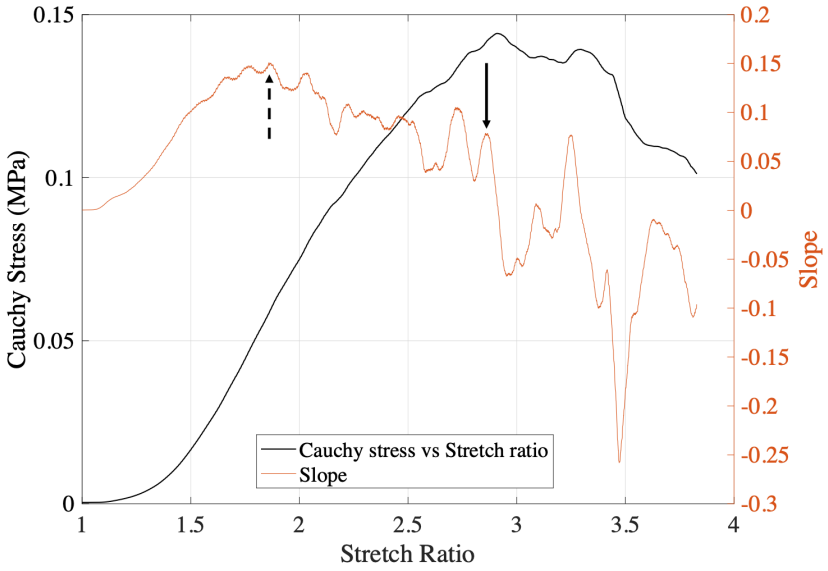

Figure 3.11: Cauchy stress vs stretch ratio plots of a calcified scaffold in black and slope curve in orange: The black dashed arrow points to the initial failure and the black solid arrow points to the final failure, Multiple failures can be seen in between initial and final failures.

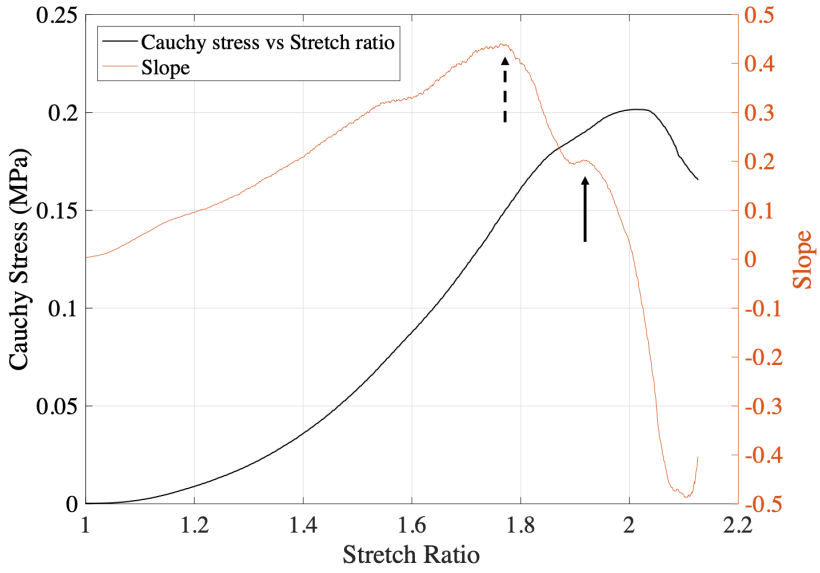

Figure 3.12: Cauchy stress vs stretch ratio plots of a non-calcified scaffold in black and slope curve in orange: The black dashed arrow points to the initial failure and the black solid arrow points to the final failure.

The stretch ratios, stresses and tangential moduli of the calcified and non-calcified scaffolds at initial and final ruptures points are listed in Table 3.1. Since the three donors were chosen for their similar osteogenic differentiation capacities and no relationships were found in the mechanical data among the donors, the mechanical data of the donors were analysed together.

Table 3.1: The stresses and stretch ratios at the initial and final rupture points, and the tangential moduli at initial rupture points are reported as median [Q1, Q3]; λ_i = Stretch at initial rupture point, λ_f = Stretch at final rupture point, σ_i = Stress at initial rupture point, σ_f = Stress at final rupture point, TM_i = Tangential modulus at initial rupture point

	Calcified scaffolds	Non-calcified scaffolds
λ_i	2.48 [2.26, 2.85]	1.73 [1.58, 1.79]
σ_i (MPa)	0.07 [0.06, 0.12]	0.08 [0.06, 0.09]
λ_f	3.73 [2.86, 4.04]	1.86 [1.79, 1.92]
σ_f (MPa)	0.11 [0.1, 0.19]	0.1 [0.09, 0.14]
TM_i (MPa)	0.13 [0.1, 0.13]	0.46 [0.29, 0.51]

The comparisons of stretch ratios at initial and final rupture points are presented in Figures 3.13(a) and (b) respectively. The stretch ratios at initial and final rupture points of calcified scaffolds were significantly higher than the non-calcified scaffolds ($p<0.05$ & $p<0.001$ respectively). Data are presented as median [Q1, Q3]. The stretch values at the initial rupture points of the calcified scaffolds, 2.48 [2.26, 2.85], start at higher values than the stretch values of the non calcified scaffolds, 1.73 [1.58, 1.79]. The same applies to the stretch values at the final rupture points, 3.73 [2.86, 4.04] and 1.86[1.79, 1.92]. The calcified scaffolds stretched to higher values before the final rupture. The non-calcified scaffolds did not reach high stretch values before final rupture.

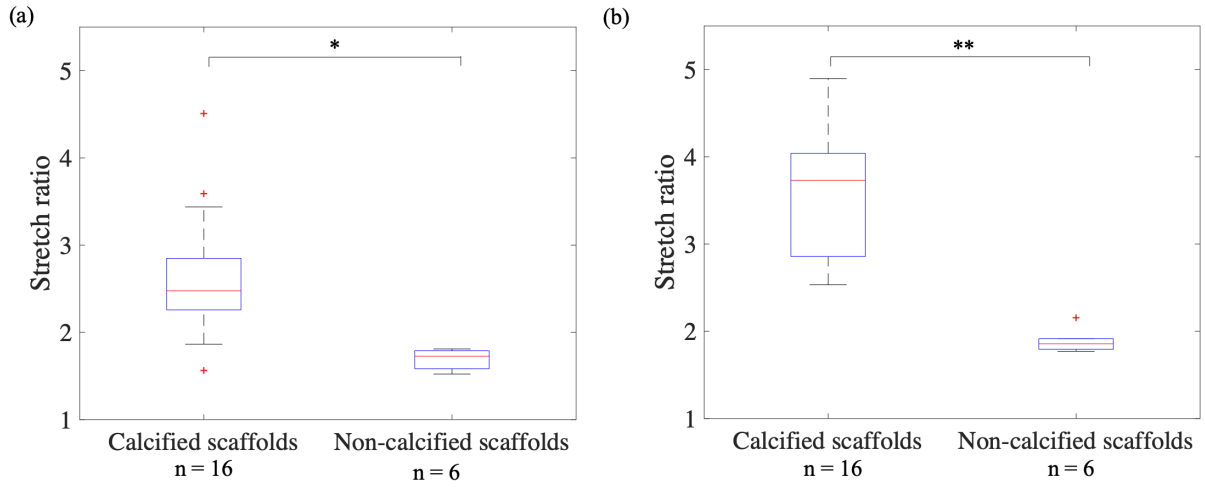

Figure 3.13: Comparisons of stretch ratios between calcified and non-calcified scaffolds at a) initial rupture points and b) final rupture points: The stretch values of calcified scaffolds at initial and final rupture points were significantly higher than non-calcified scaffolds; * : $p<0.05$, ** : $p<0.001$.

The comparisons of stresses at initial and final rupture points are presented in Figures 3.14(a) and (b) respectively. The stresses at the initial rupture points of calcified scaffolds, 0.07 [0.06, 0.12] were statistically comparable ($p = 0.858$) to the non calcified scaffolds, 0.08 [0.06, 0.09]. The stresses at the final rupture points of calcified and non-calcified scaffolds were also statistically comparable ($p = 0.261$), 0.11 [0.1, 0.19] & 0.1 [0.09, 0.14] for calcified and non-calcified scaffolds respectively. Although the values were not significantly different, the stresses at the initial and final rupture points of some of the calcified scaffolds were still higher than the non-calcified scaffolds.

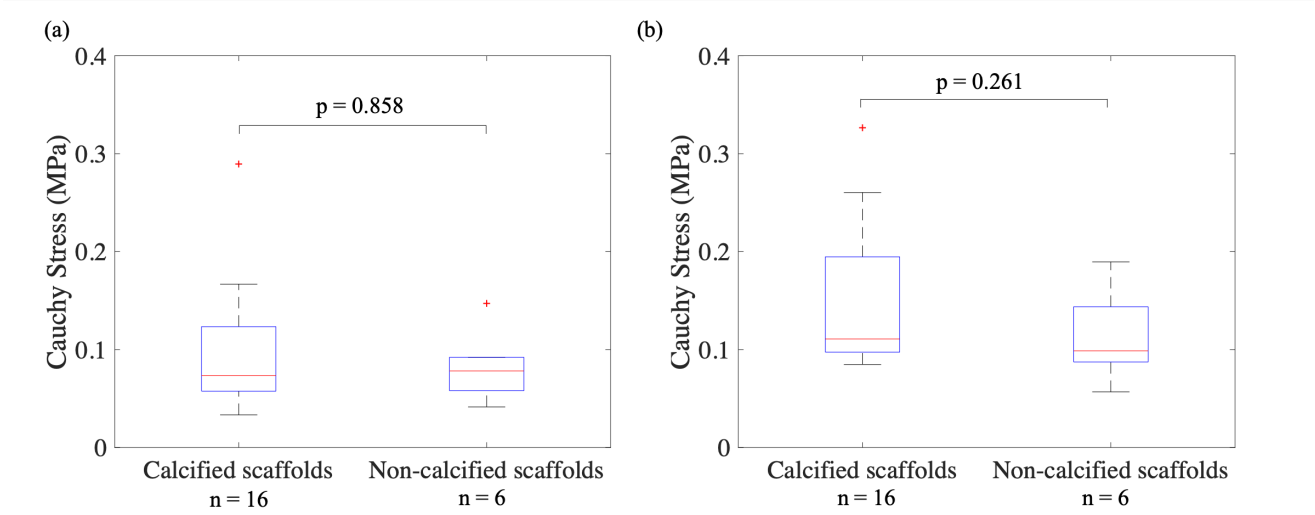

Figure 3.14: Comparisons of stresses between calcified and non-calcified scaffolds at (a) initial rupture points and (b) final rupture points: The stresses of calcified scaffolds at initial (p = 0858) and final rupture points (p = 0.261) were statistically comparable to non-calcified scaffolds.

The comparison of tangential moduli at initial rupture points between calcified and non-calcified scaffolds is presented in Figure 3.15. The tangential moduli were calculated at the stretch values at initial rupture points. The non-calcified scaffolds had significantly higher tangential moduli ($p<0.001$). The non-calcified scaffolds exhibited a stiffer response than the calcified scaffolds.

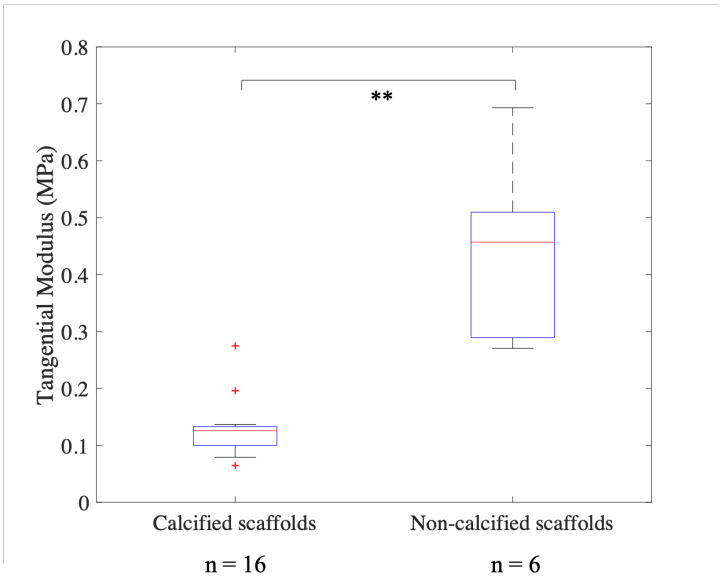

Figure 3.15: Comparisons of tangential moduli between calcified and non-calcified scaffolds at initial rupture points: The tangential moduli values of non-calcified scaffolds were significantly higher than calcified scaffolds; ** : $p<0.001$.

3.2.4. Comparing the calcified scaffolds to atherosclerotic fibrous caps

Three studies have carried out uniaxial tensile tests on fibrous caps. Loree et al [26] tested 26 fibrous caps harvested from aortic plaques. Five of the fibrous caps classified as calcified were used for comparison. Holzapfel et al [27] tested 9 fibrous caps (fibrotic part at the luminal border) harvested

from iliac arteries. Teng et al [24] tested 59 fibrous caps harvested from carotid arteries. The average curves calculated over the strain energy of each study is plotted with this study's average curve. The three studies report similar results for the fibrous caps. This study's calcified scaffolds displayed a high stretch and low stress at failure compared to the three studies. The fibrous caps were a lot stiffer than this study's calcified scaffolds.

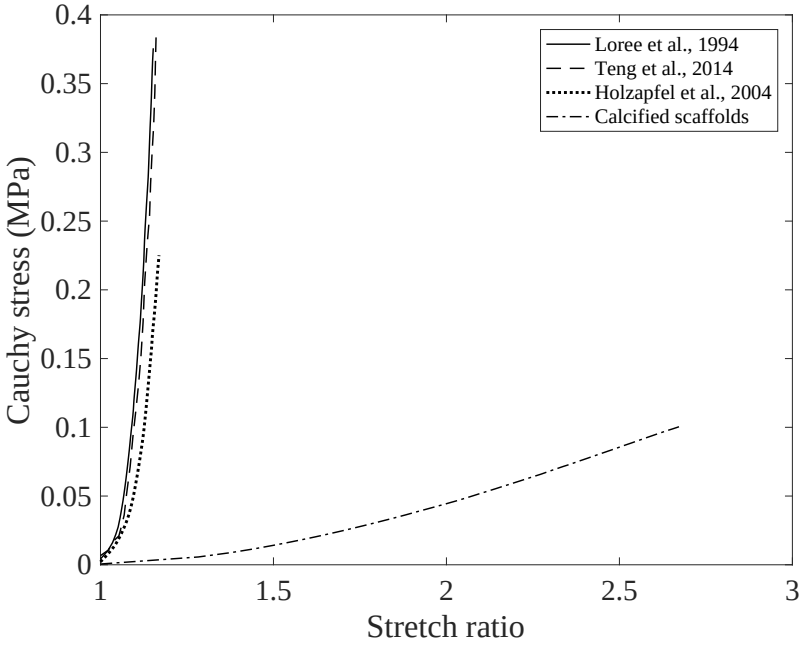

Figure 3.16: Comparison of Loree et al [26], Teng et al [24] and Holzapfel et al [27] averaged data of fibrous caps with this study's averaged data of the calcified scaffolds.

To summarise, the calcified scaffolds and non-calcified scaffolds exhibited distinct mechanical behaviours. The calcified scaffolds exhibited a wide variation in mechanical behaviours. A wider range in stretch ratios and stresses were observed in the calcified scaffolds than the non-calcified scaffolds. The calcified scaffolds exhibited higher stretch ratios at initial and final failure points. Calcified scaffolds were more compliant than the non-calcified scaffolds.

3.3. Morphology and Failure

The structure of the calcified and non-calcified scaffolds were studied through histology and scanning electron microscopy (SEM). In this section, the results of these analyses are presented.

Out of the sixteen calcified scaffolds tested, two scaffolds were analysed using SEM and fourteen were processed for histology i.e. sectioning and various stains. Out of the 6 non-calcified scaffolds tested, one scaffold was analysed using SEM and five were processed for histology. To study the failure behaviour of a scaffold, the histological sections at different thickness would have to be studied. This way the failure can be tracked through the thickness. Due to difficulties faced during sectioning, sections through the thickness and preserving the length and width could not be obtained. Care was taken to ensure that at least one section at a thickness for each stain was attained. Due to the lack of sections through the thickness of the scaffold, the failure behaviour could not be studied effectively since the morphology and composition of the scaffolds changed with the thickness. This served as a limitation to carry out a complete quantitative analyses such as measuring the number of cells, calcium phosphate deposits or density of collagen fibres in the entire collagen scaffold. Only 4 calcified scaffolds could be analysed quantitatively for the amount of calcium phosphate deposits at one thickness. Hence, qualitative analyses were also carried out on the 4 calcified scaffolds. The non-calcified scaffolds were only analysed qualitatively. Visual observations made on the test images taking during the mechanical tests, histology images and scanning electron microscopy images are discussed below.

3.3.1. Morphology

An overview of the scaffolds stained by different staining methods is presented here. Calcified and non-calcified scaffolds were stained using three types of stains: Von Kossa, Miller and H&E. H&E staining was used to observe the cells distributed in the scaffolds. Miller and Von Kossa staining were used to analyse collagen fibres and calcium phosphate deposits respectively. Since Von Kossa stains the deposits, there were no Von Kossa stains of the non-calcified scaffolds. An example of a Miller stain of a non-calcified scaffold is included in the Appendix A.5. A representative H&E stain of a calcified scaffold whose entire length was preserved is shown in Figure 3.17. The regions of the scaffolds under the clamps are marked in grey. During any analysis of the histology images, the clamps were excluded. Representative H&E stains, Miller stains and Von Kossa stains of ruptured regions in the calcified scaffolds at a higher magnification are illustrated in Figures 3.17(b-d). Approximately the same representative regions marked by the black box in Figures 3.17(a) were considered for each stained images.

An H&E stain is shown in Figure 3.17(b). Cells were distributed throughout each scaffold at different densities. Higher concentrations of cells were seen in some regions and few cells were seen in other regions. Cluster of cells and random distributions of cells, pointed out by the black solid arrow were seen. The collagen fibres are pointed out the black dashed arrow.

A Miller stain is shown in Figure 3.17(c). In a Miller stain, collagen fibres stain purple. It can also be used to visualise cells which stain brown. The black dashed arrow points to the collagen fibres. The cells, pointed out by the black solid arrow, were also seen in the same region of the H&E stain as shown in Figure 3.17(b).

A Von Kossa stain is shown in Figure 3.17(d). Deposition of calcium phosphate was confirmed by positive Von Kossa staining. The deposits were distributed throughout the scaffold with varying concentrations. As pointed out by the orange arrow, there were more deposits in some regions than the other regions. The size (diameter) of the calcium phosphate deposits varied from 1.01 μm to

53.31 μm with an average size of 6.45 μm.

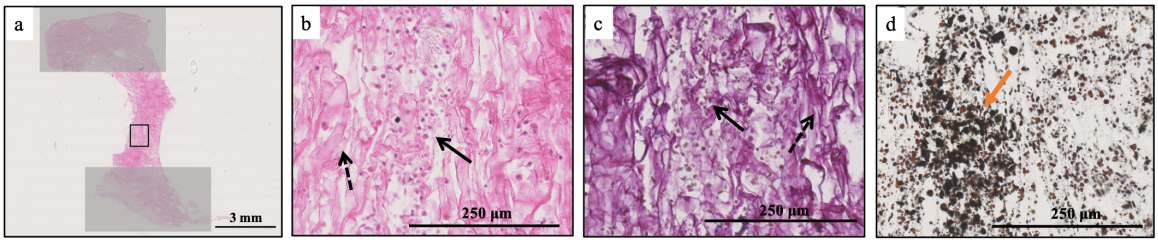

Figure 3.17: Representative H&E, Miller and Von Kossa stained images of a calcified scaffold: (a) Overview of the entire H&E stained scaffold, (b) H&E stain at a higher magnification: Black solid arrow points to cells, black dashed arrow points to collagen fibres (c) Miller stain at a higher magnification: Black solid arrow points to cells, black dashed arrow points to collagen fibres, (d) Von Kossa stain at a higher magnification: Orange arrow points to a concentration of deposits.

Thionin staining was also done with the Von Kossa stain to detect cells. The cells stain blue with Thionin staining as pointed out by the black arrow in Figure 3.18.

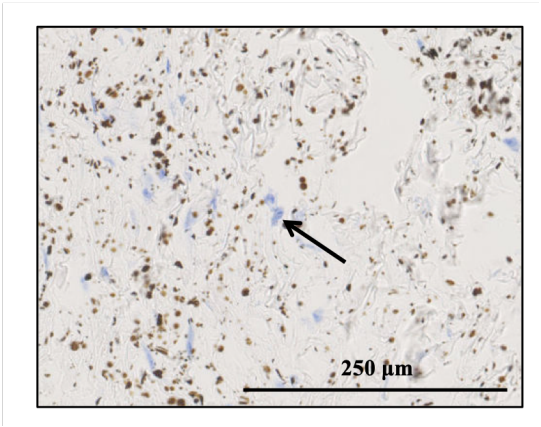

Figure 3.18: Thionin staining done along with Von Kossa stain: Cells stain blue, pointed by the black solid arrow.

Calcium phosphate formation

In Figure 3.19, the translucent lines are the collagen fibres. Since Von Kossa staining only highlights calcium compounds, the collagen fibres do not stain. Deposits of calcium phosphate seemed to form along or on these translucent collagen fibres. They did not seem to form in the pores between the collagen fibre matrix.

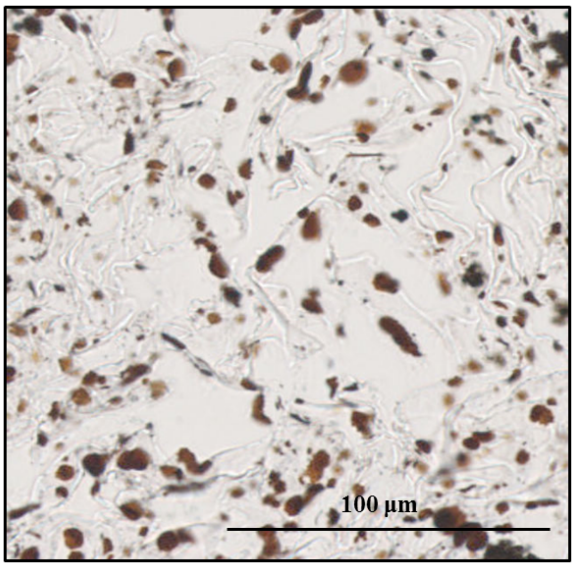

Figure 3.19: Von Kossa stain of calcified scaffold at a high magnification: Deposits of calcium phosphate seem to be forming along/on collagen fibres.

3.3.2. Failure

The images taken during the tensile tests were analysed visually to study and characterise the failure behaviour of the calcified and non-calcified scaffolds. The calcified scaffolds and non-calcified scaffolds exhibited different failure behaviours. Representative images of the two observed failure behaviours are presented in Figure 3.20. The images show the state of the scaffold at the end of the tensile test. Failure refers to a macroscopic observation of a rupture occurring in the scaffold. The failure behaviour of the non-calcified and calcified scaffolds are described below.

Non-calcified scaffold's failure behaviour: Rupture occurred through the thickness of the scaffold. Once a rupture occurred in the scaffold, it quickly led to the overall failure of the scaffold. The rupture propagated through the thickness of the scaffold. This is pointed out by the white arrow in Figure 3.20(a). The scaffold did not stretch considerably before failure.

Calcified scaffold's failure behaviour: In this type of failure, two observations were made. Firstly, it was observed macroscopically that some fibres in regions of the scaffold ruptured. In these regions, the fibres that did not rupture, stretched considerably. This led to a reduction in thickness as seen by translucent areas. One such region is marked with R in Figure 3.20(b). Secondly, it was also observed macroscopically that in some regions, the fibres didn't rupture or stretch. The fibres in these regions looked like they stayed intact. There could have been failures in the intact areas which were not visible. Such an intact regions is marked with I in Figure 3.20(b). This type of failure can be described as the stretch being directed to certain parts of the scaffold. The brown spots on the scaffold in Figure 3.20(b) are remnants from attempts made for digital image correlation (DIC).

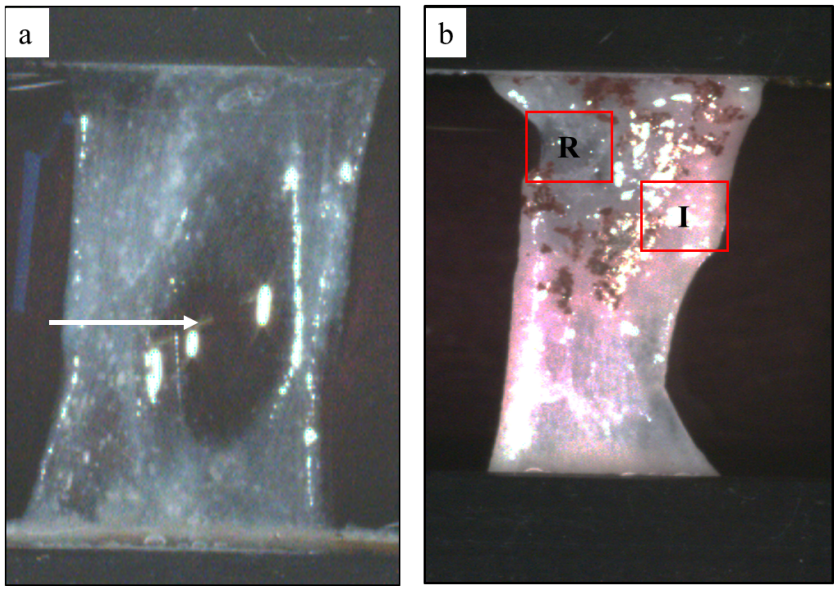

Figure 3.20: Images of the final state of ruptured scaffolds during tensile test: (a) Non-calcified scaffolds: Ruptured through the thickness of the scaffold, pointed out by the white arrow, (b) Calcified scaffolds: Fibres in parts of the scaffold visibly ruptured and stretched (marked with R), and other parts of the scaffold visually remained intact (marked with I).

The failure behaviour of the calcified scaffolds was studied using the Miller stain. In Figure 3.21(a), the same image of the ruptured calcified scaffold at the final ruptured state during the tensile test is shown. The corresponding Miller stain of the scaffold, marked with the same ruptured and intact regions, is shown in Figure 3.21(b). To analyse the morphology of the collagen fibres, a comparison was made between the stretched fibres in the ruptured regions (R) and the fibres that didn't stretch in the intact regions (I) of the scaffold. In Figure 3.21(c & d), images at a higher magnification of the regions marked R and I are shown respectively. The black arrow indicates the direction of pull during the tensile test. In Figure 3.21(c), the collagen fibres that stretched in the ruptured regions aligned in the direction of the pull. In Figure 3.21(d), the collagen fibres in the intact regions did not align in the direction of the pull. The random network of collagen fibres was preserved. The density of the collagen fibres in the ruptured regions appeared to be less compared to the intact regions.

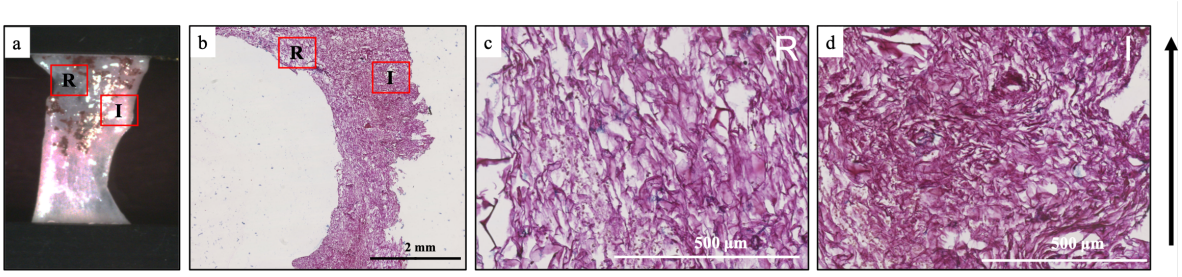

Figure 3.21: Studying the failure behaviour through the morphology of collagen fibres in ruptured calcified scaffolds: (a) Final ruptured state of a calcified scaffold during tensile test, (b) Corresponding Miller stain of ruptured scaffold at a low magnification, (c) Collagen fibres aligned in the direction of pull, (d) Random collagen fibre network preserved; R: rupture region, I: intact region, Black arrow indicates direction of pull during tension test.

The corresponding ruptured and intact areas analysed by the Miller stain were analysed using the Von Kossa stain. The entire intact area in the scaffold is marked in yellow in Figure 3.22(a). The corresponding Von Kossa images at different thicknesses through the scaffold are shown in Fig-

ure 3.22(b) & (c). In Figure 3.22(b), the entire intact area is roughly marked with a black box. Majority of the fibres ruptured in the areas not marked by the box. The total amount of deposits was observed to be higher in this intact marked area than the ruptured areas. Similarly, in Figure 3.22(c), another intact area is marked with a black box. The overall amount of calcium phosphate deposits in the intact areas of Figures 3.22(b) & (c) together seemed to be higher than the ruptured areas. It can be appreciated from Figures 3.22(b) & (c) that the amount of deposits varies through the thickness of the scaffold.

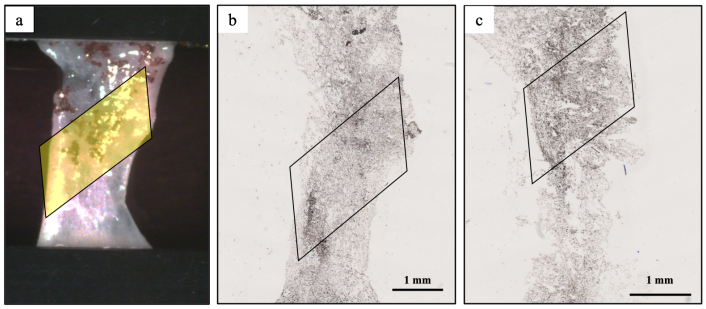

Figure 3.22: Representative images to analyse calcium phosphate deposits in ruptured a calcified scaffold: (a) Final ruptured state of a calcified scaffold during tensile testing, with intact area marked in yellow, (b & c) Corresponding Von Kossa stained images at different thicknesses with the intact areas marked with a black box.

Comparing stresses and stretch ratios to the amount of calcium phosphate deposits

To quantify the amount of calcium phosphate deposits, only histologic sections with the entire length of the collagen scaffold preserved were analysed. This ensured that an overview of the distribution of the deposits could be attained. This analysis did not account for the variation of the deposits through the thickness. The area fractions of calcium phosphate deposits were calculated in four scaffolds. The plots of area fractions of each scaffold against their final stretch ratios and final stresses are shown in Figures 3.23(a)&(b) respectively. The scaffolds are numbered from 1 to 4. Scaffolds 3 and 4 had the highest area fractions and scaffolds 1 and 2 had the lowest area fractions. It suggests that a higher calcium phosphate content resulted in a higher stretch at final failure. No relations were observed between the area fractions and the stresses at final failure. The Cauchy stress vs stretch ratio plots of the four calcified scaffolds till their final failures and their corresponding Von Kossa stains are shown in Figure 3.24(a-d). Their initial failures are marked with a black dashed arrow. The scaffolds 3 and 4 in the graphs of Figures 3.24(c)&(d) seemed to exhibit more failures in between the initial and final failures, than the scaffolds 1 and 2. These failures are marked with a black bracket. After the initial failures in the scaffolds 1 and 2, similar noticeable failures were not observed in the graphs of Figures 3.24(a) & (b). Scaffold 4 in Figure 3.24(d), which had the highest calcium phosphate area fraction exhibited more failures between the initial and final failures than scaffold 3. This seemed to suggest that the calcium phosphate deposits played a role in these failures. No relations were observed between the area fraction and stresses and stretch ratios at initial failures. The sample size (n = 4) is a limitation.

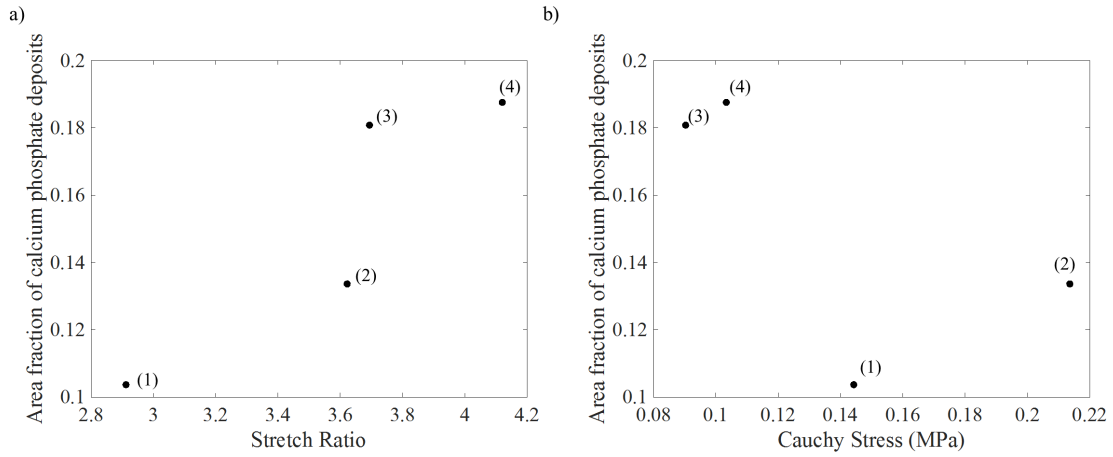

Figure 3.23: Scatter plots at final failures of: (a) Area fractions of calcium phosphate deposits vs stretch ratios, (b) Area fractions of calcium phosphate deposits vs Cauchy stresses; Numbers (1-4) correspond to scaffold numbers.

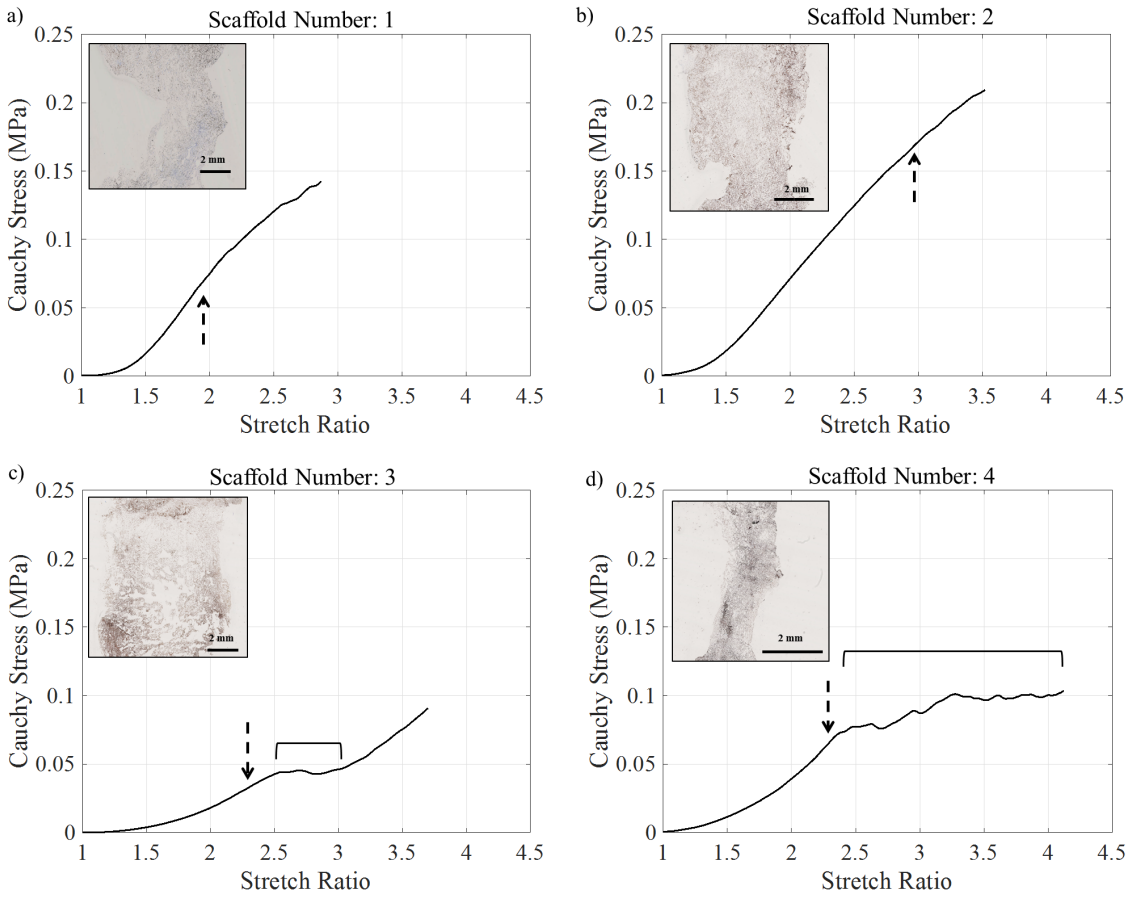

Figure 3.24: Cauchy stress vs stretch ratio plots of the four calcified scaffolds until final failures with their corresponding Von Kossa stains: (a-d) Ascending order of calcium area fraction and stretch ratios; Black dashed arrows point to initial failures, Black brackets marks the multiple failures.

Scanning Electron Microscopy (SEM)

The calcified and non-calcified scaffolds were analysed using the scanning electron microscope (SEM) to investigate their failure. To characterise the scaffolds before the mechanical tests were carried out, a non-calcified scaffold and a calcified scaffold were imaged. A non-calcified scaffold and a calcified scaffold before tensile testing are shown in Figure 3.25(a) & Figure 3.25(b) respectively. These images were taken from the top surfaces of the scaffolds. The scaffold in Figure 3.25(a) represents the state of a scaffold before any cells are seeded on it while the scaffold in Figure 3.25(b) represents the state of a scaffold at the end of cell culture. The non-calcified scaffold is highly porous with a porosity of 99.51% [34]. This can be seen in Figure 3.25(a). This is better seen in the cross section image in the inset, adapted from Matrsiko et al [34]. From the inset, it was observed that the collagen fibres form a continuous porous network. As mentioned earlier, during culture, the calcified scaffolds shrank by approximately 50%. As seen in Figure 3.25(b), the calcified scaffold is denser. The porosity of the scaffold has decreased considerably. The collagen network appears to have buckled. Distribution of calcium phosphate deposits were also seen as pointed out by the orange arrow. The structure of the collagen fibres in the calcified scaffolds seem to be affected as well. Fibres of different thicknesses were seen as pointed out by the blue arrows. The fibre network appeared to be disrupted.

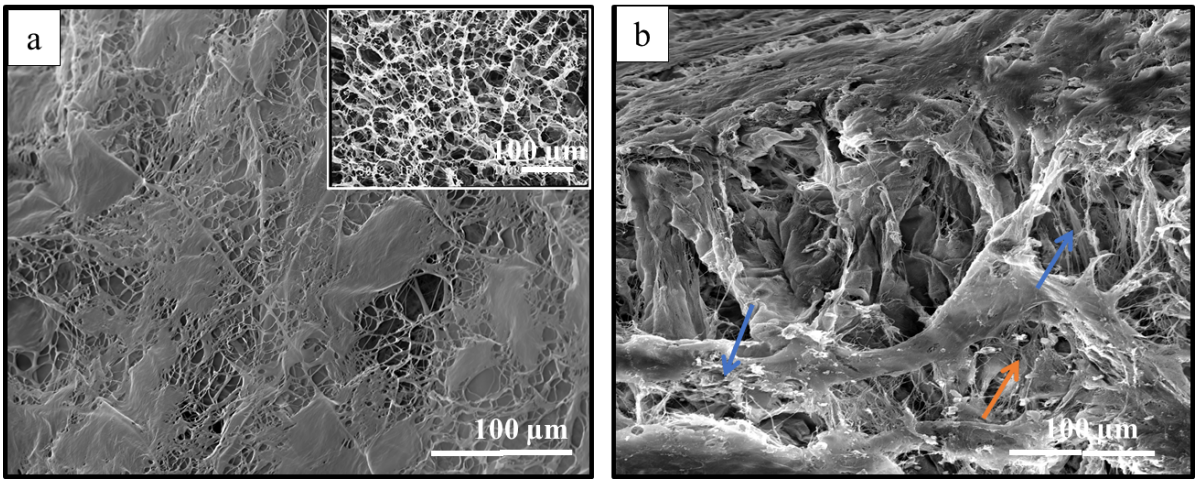

Figure 3.25: Scanning Electron Microscopy images of the top surfaces of a non-calcified and calcified scaffold before mechanical testing: (a) Highly porous non-calcified scaffold, inset: Image taken from cross-section, adapted from Matrsiko et al. [34] (b) Less porous calcified scaffold at the end of culture.

In Figures 3.26(a), an image of a ruptured calcified scaffold stretched apart but not completely separated into two pieces, with two areas of interest marked are shown. The orange double headed arrow marks the region where the fibres ruptured completely leading to separation while the black double headed arrows mark the regions where majority of the fibres stretched considerably but did not rupture. In the Figure 3.26(a), the region of the scaffold, where majority of the fibres stretched but didn't rupture, is marked with a black dashed box. In Figures 3.26(b) & (d), the same region is shown at higher magnifications. Two kinds of ruptures of the collagen fibres were observed. Most of the fibres on the surface ruptured and retracted as indicated by black solid arrows in Figure 3.26(b). The fibres, below the ruptured fibres, stretched considerably but did not rupture as indicated by the black dashed arrows in Figure 3.26(b). In Figure 3.26(d), a clearer impression was attained. The collagen fibres appeared as thick ribbons. As pointed out by the black solid arrow, when these ribbons were stretched, the ribbons separated into thinner fibres. In some cases, as pointed out by the

black dashed arrow, the thinner fibres ruptured completely leading to the complete failure of the thick ribbon like collagen fibres. Rupturing of the fibres was characterised by considerable thinning down of the fibres. The stretched fibres aligned in the direction of pull.

In the Figure 3.26(a), the region of the scaffold, where majority of the fibres ruptured, is marked with an orange dashed box. In Figures 3.26(c) & (e), the same region is shown at higher magnifications. As indicated by the black solid arrows, the fibres thinned down considerably while rupturing. The fibres didn't seem to stretch as much, pointed out by the black dashed arrows. In Figure 3.26(e), it could be seen clearly that there were a lot of thin fibres. The fibres didn't align in the direction of pull.

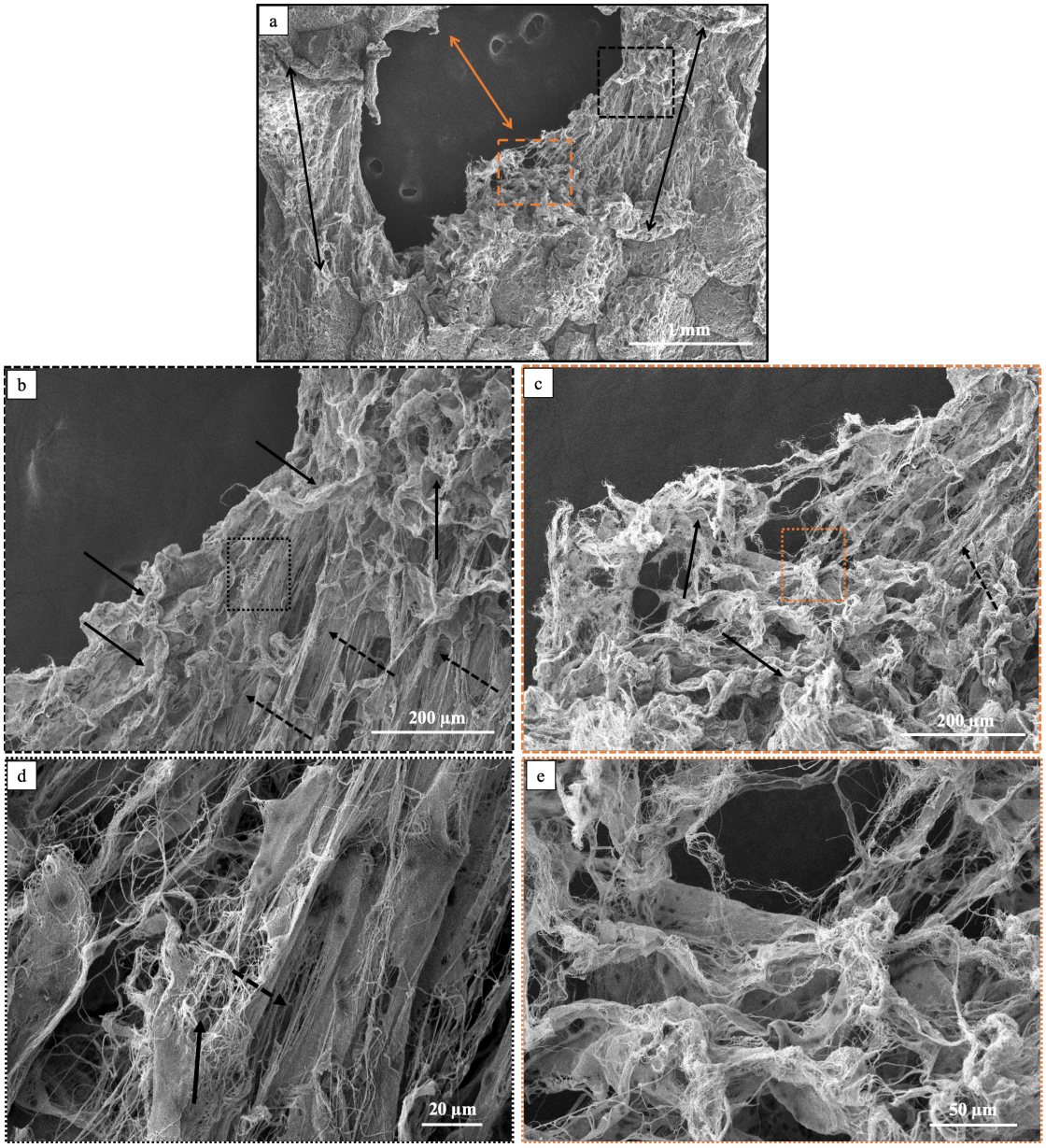

Figure 3.26: Scanning Electron Microscopy images of a mechanically tested calcified scaffold, stretched apart but not completely separated into two pieces: (a) Overview image: Black marks the region where majority of the fibres stretched but didn't rupture, Orange marks the region where the scaffold ruptured and separated, (b) & (d) Higher magnification images of the areas marked with the black box, (c) & (e) Higher magnification images of the areas marked with the orange box; Black dashed and solid arrows point to fibres that stretched and ruptured respectively

Images taken from the cross section of a scaffold that was pulled till it was completely separated are shown in Figures 3.27. The collagen scaffold didn't separate evenly through the width. In Figure 3.27(a), the surface appears to be uneven. The denser nature of the calcified scaffold was even more evident in the Figures 3.27(b). Some regions have a highly compacted fibre network while in some regions, the fibre network looks more loosely packed. Thinning of fibres was observed. Some calcium phosphate deposits were seen scattered around the fibres as pointed out by the black arrows.

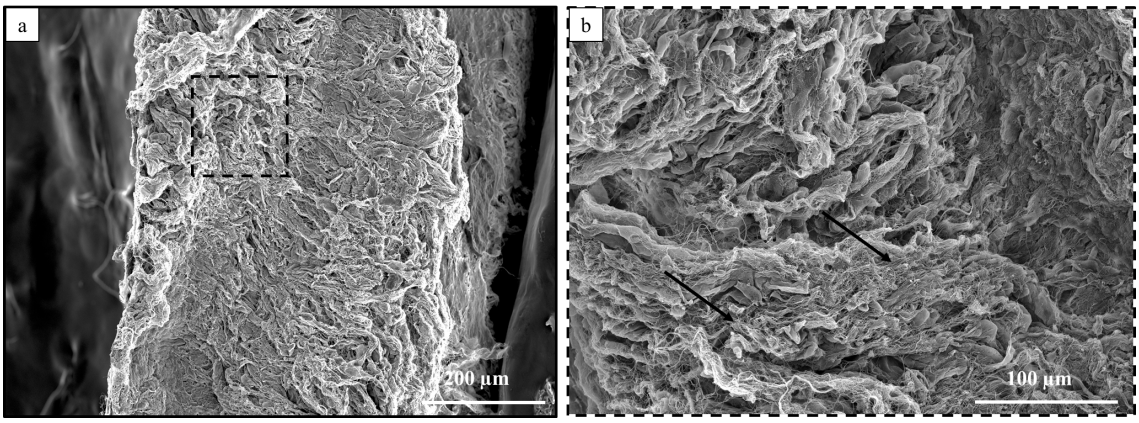

Figure 3.27: Scanning Electron Microscopy images of a mechanically tested calcified scaffold, stretched apart till complete separation, taken from the cross-section: (a) Overview image, (b) Higher magnification of marked region: Dense collagen network, Black arrows point to some calcium phosphate deposits.

In Figure 3.28, images of a ruptured non-calcified are shown. The collagen fibre network was looser in the non-calcified scaffolds. This can be seen in the higher magnification image in Figure 3.28(b). It was observed that the fibres didn't stretch as much as the calcified scaffold. The ribbon like nature of the fibres was more evident in these images as pointed out by the black dashed arrow. It appeared as though the ribbons ruptured without thinning down as much as the fibres in the calcified scaffolds. The thinning is pointed out by the black solid arrow.

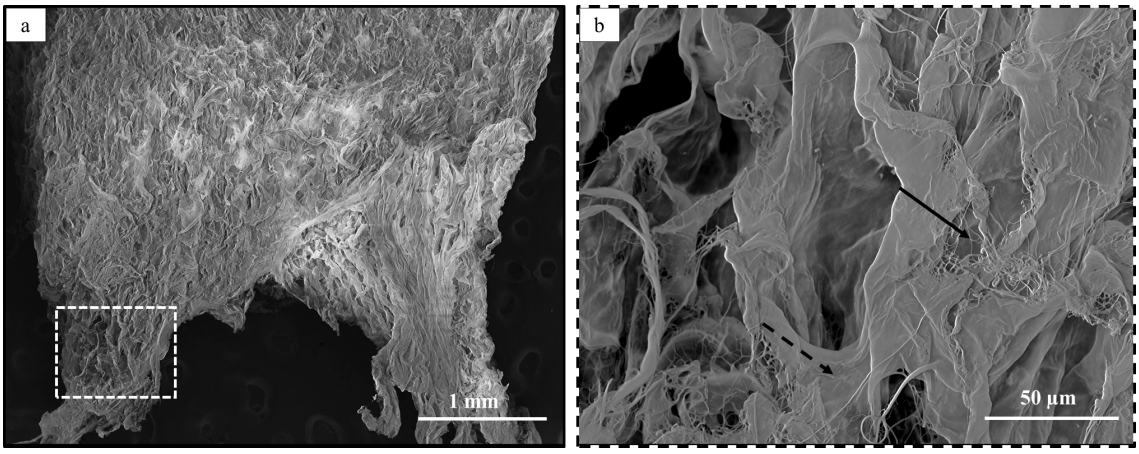

Figure 3.28: Scanning Electron Microscopy images of a mechanically tested non-calcified scaffold: (a) Overview image, (b) Higher magnification image of marked region: Black dashed arrow points to collagen fibre ribbon, Black solid arrow points to thinned down fibres.

Calcium phosphate deposits of varying sizes were seen distributed in the scaffolds. They seemed to be entangled within the collagen fibres, indicated by the white dashed arrow and/or sitting on the

collagen fibres, indicated by the white solid arrow. The deposits looked like they were well integrated in the collagen fibre network.

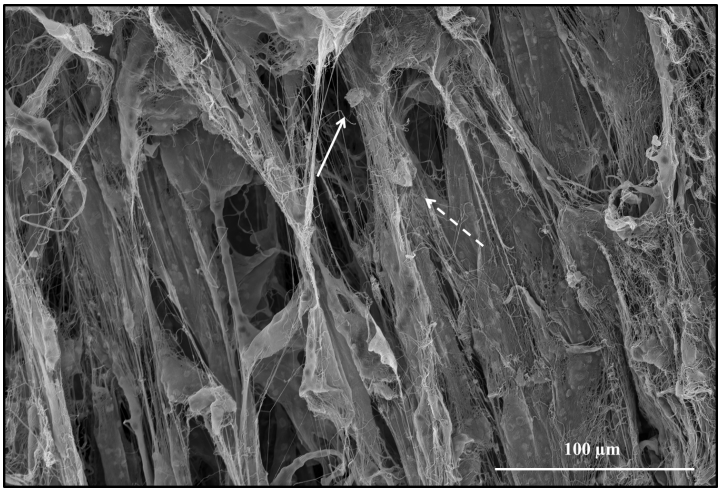

Figure 3.29: Scanning Electron Microscopy image to highlight the calcium phosphate deposits in the collagen fibre network: White dashed arrow points to a deposit entangled in the fibres, white solid arrow points to a deposits sitting on the fibre.

Energy-dispersive x-ray spectroscopy (EDX) was carried out on the calcified scaffolds to detect the elemental composition of the calcium phosphate deposits. Twelve locations of the calcified scaffolds were analysed. An example of the line analysis is included in the Appendix A.6. A wide variation was detected in the composition of the deposits. The atomic Ca/P ratio was on average 1.49 $\pm$ 0.45, ranging from 1.18 to 1.42 and 2.15 to 2.66. The atomic ratios of the calcium phosphate deposits correlated with those of amorphous calcium phosphate. In Figure 3.30, one of the elemental map analyses carried out is shown. In Figure 3.30(a), the area over which the scan was carried out is shown. The colours, red and blue indicate the distribution of calcium and phosphorus atoms in Figures 3.30(b) & (c) respectively. The Ca/P ratio was 1.44. It can be seen that there is a distribution of the elements all over the scaffold, with concentrations at the top right corner. The amount of phosphorous seemed to be more than calcium. This highlights the distribution well since the deposits can not be seen clearly seen in Figure 3.30(a). This also indicates that there were deposits possibly at all the rupture sites which couldn't be seen clearly. The corresponding spectra is shown in Figure 3.30(d). The peaks relating to Ca and P are circled in red.

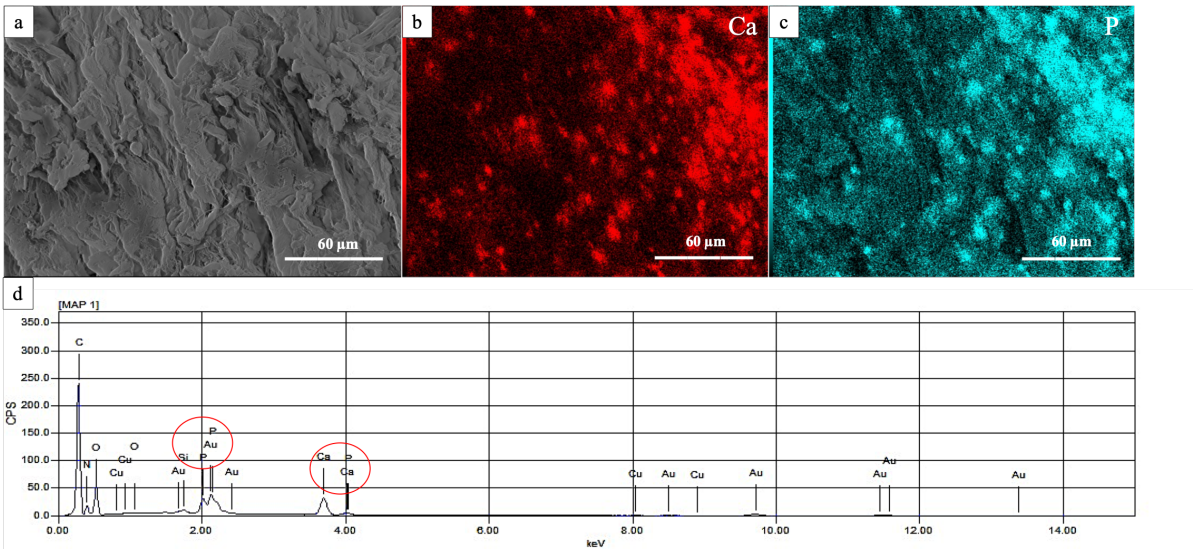

Figure 3.30: Element map of an area on the calcified scaffold: (a) Scanning Electron Microscopy image of an area of interest, (b) Red indicates the distribution of calcium atoms, (c) Blue indicates the distribution of phosphorous atoms, (d) Corresponding spectra with Ca and P peaks circled in red.

In Figure 3.31(a) & (b), the EDX spectra of the point analysis carried out at rupture sites are shown. Point 1 refers to a deposit found in an area where the scaffold stretched and Point 2 refers to a deposit found in an area where the scaffold ruptured. There was quite a big variation in the composition of the two deposits. Point 1 had a Ca/P ratio of 2.15 and Point 2 had a Ca/P ratio of 1.22.

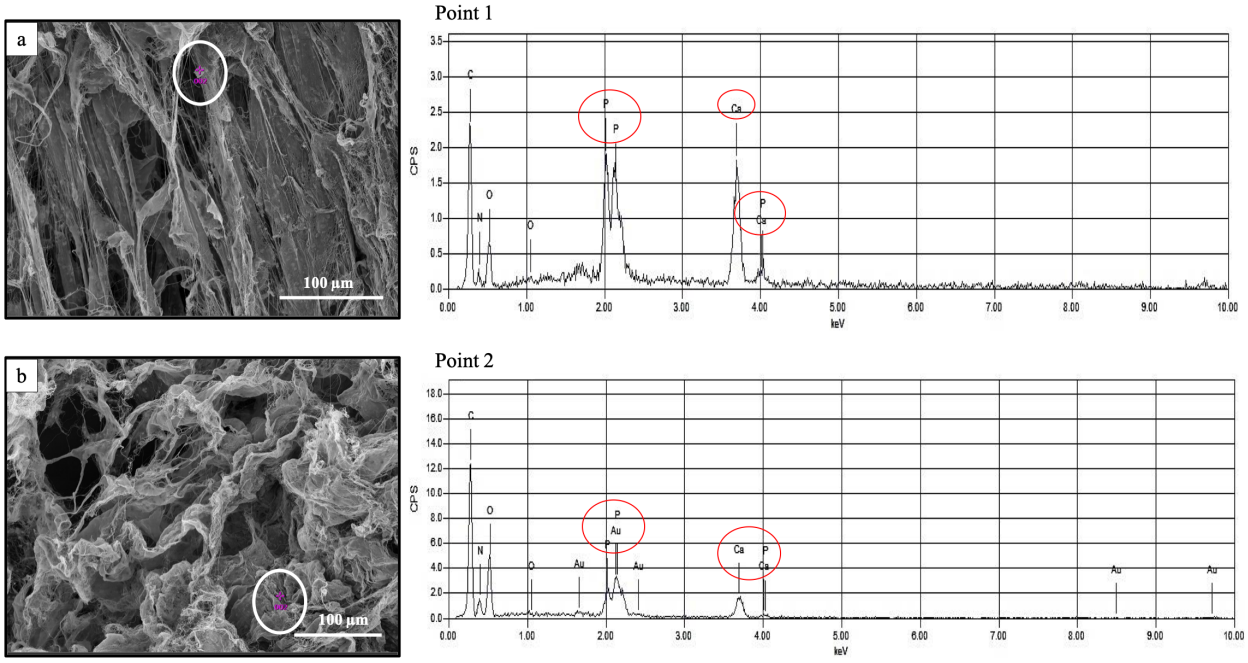

Figure 3.31: Energy-dispersive X-ray spectroscopy on an area where majority of the fibres: (a) stretched and its corresponding spectra, (b) ruptured and its corresponding spectra; red circles indicate the Ca and P peaks.

The atomic percent of all the elements detected by the EDX in the element map and the two point analyses are listed in table 3.2.

Table 3.2: Atomic percent of all elements detected by EDX by elemental mapping and at the two points in the calcified scaffolds.

	Map	Point 1	Point 2
C	65.82	60.94	61.88
N	6.00	4.33	8.03
O	25.39	22.13	25.28
Si	0.17	-	-
P	0.86	3.99	1.59
Ca	1.24	8.61	1.94
Cu	0.03	-	-
Au	0.49	-	1.27
Ca/P	1.44	2.15	1.22

To summarise, calcium phosphate deposits formed through the volume of the scaffold at different concentrations. The calcified and non-calcified scaffolds failed in different manners. Through qualitative analyses, some effects of the deposits on the ruptured structure were observed. The elemental composition of the deposits (Ca/P) had an average of 1.49 ± 0.45 ranging from 1.18 to 2.66.

4

Discussion

The aim of this study was to create collagen scaffold constructs with calcifications intended for the development of an in-vitro model of an atherosclerotic fibrous cap. Collagen type 1 scaffolds were seeded with paediatric MSCs (p-MSCs) to create calcium phosphate deposits. These collagen scaffold constructs were mechanically tested by uniaxial tension tests to study the mechanical properties. Histology and scanning electron microscopy were used to characterise the failure behaviour.

4.1. Calcified scaffolds: Fabrication and Composition

4.1.1. Cell culture

Three cell seeding methods were attempted since the initial attachment of cells to a scaffold is essential for a successful tissue engineered construct [44]. The ideal technique to seed MSCs on 3D matrices is unclear since seeding techniques, the structure and material of the scaffolds influence the initial attachment of MSCs [45]. Out of the three methods attempted, semi-passive seeding was found to be the most optimal. The semi-passively seeded scaffolds showed higher cellularity potentially due to the mechanical forces which enabled the cells to infiltrate the scaffolds at a higher and faster rate [48]. Passive seeding may have been the least successful due to the lack of these forces. In the semi-passive seeding method, the structural integrity of the scaffolds was preserved. The scaffolds were not vigorously shaken in the semi-passive seeding method, as seen in the dynamic seeding method.

The use of external forces to aid cells' infiltration of the scaffolds can be explained by the intrinsic behaviour of stem cells. Stems cells and their surrounding micro-environment communicate using mechanical cues. These cues help regulate cell fate, behaviour, proliferation, self-assembly and organisation. In the human body, biological tissues transmit forces which regulate stem cell function, guide development and tissue repair [46]. If human in-vitro models of organs and diseases are to be made, these forces have to be duplicated as well. Extrinsic forces can be applied to stems cell to influence their intrinsic behaviour. In this way, the cells can proliferate in conditions similar to the human body. For tissue engineering, mechanical forces that mimic the forces experienced by cells in-vivo might enhance cell migration. Dynamic conditions improve cell seeding by increasing the chances of cell-scaffold contact [47]. The semi-passive method manages to find the right balance between using mechanical forces for cell migration and maintaining the structure of the matrix.

4.1.2. Shrinkage due to cells

By the end of culture, the calcified scaffolds had shrunk by approximately 50% from their original size. The collagen scaffold buckled under the forces of the cells seeded on the scaffolds. The collagen scaffolds before seeding had a high porosity of 99.6% [34]. This was observed in the Figure 3.25(a). A decrease in porosity was observed in the calcified scaffold as shown in Figure 3.25(b). This meant that the calcified scaffolds had more material than the non-calcified scaffolds of the same dimensions. Also, in Figure 3.25(b), the structure of the collagen fibres seemed to be affected by the cells and/or the calcium phosphate deposits. The shrinkage was caused due to the cells seeded on the scaffolds. A mechanical interplay exists between the cells and scaffold's properties. Cells can generate quantifiable contractile forces that lead to scaffold contraction [49]. Cells seeded on collagen hydrogels can buckle under the contractile forces of the cells resulting in contraction [50].

4.1.3. Calcium phosphate deposits

The calcium phosphate deposits and its effect on the collagen scaffolds are compared to calcifications found in atherosclerotic tissues. Ca/P atomic ratios of the deposits found in the calcified scaffolds varied from deposit to deposit, ranging from 1.18 to 1.42 and 2.15 to 2.66 with an average of 1.49 ± 0.45. The Ca/P atomic ratios indicate that the deposits could be amorphous calcium phosphate (ACP) [51]. This is in line with the formation of calcifications during atherosclerosis. Ca-rich material deposits in the intima of an artery early in the disease [51]. Calcification progresses with amorphous calcium phosphate depositions which mature with time to transform into crystalline hydroxyapatite (HAp). ACP is the initial solid phase to form. This finally forms into calcified spherules [52]. It has also been found that spherical aggregates of ACP do not always transform to HAp. Both ACP and HAp have been found [52]. In the study by Roijers et al, the Ca/P mass ratio of the microcalcifications found in their study corresponded to ACP rather than pure HAp. The calcium phosphate deposits were not hydroxyapatite (HAp) crystals which have an atomic ratio of 1.67. Despite the ambiguity in the composition of calcifications, the calcium phosphate deposits formed in this study were in agreement with the calcification process seen in atherosclerotic plaques. A destabilising diameter range of 5 μm - 15 μm has been suggested through biomechancial studies [13, 15–17]. In this study, the calcium phosphate deposits had an average size of 6.45 μm, ranging from 1.01 μm to 53.31 μm. Hence, a collagen scaffold construct with calcium deposits in the destabilising range, comparable to atherosclerotic fibrous caps, was successfully created.

4.2. Mechanical properties

Differences were seen in stretch ratios and tangential moduli between the calcified and non-calcified scaffolds. Since the structure and composition of the calcified and non-calcified scaffolds differed based on the cells and calcium phosphate deposits, it can be inferred that they had an effect on the calcified scaffold's mechanical behaviours. Calcifications have a high stiffness, with an average Young's Modulus of 690 ± 2300 MPa and values ranging from 100 MPa to 10 GPa, even going as high as 21 GPa [53]. This high stiffness of calcifications leads to dissimilarities in the material properties with the surrounding fibrous tissue.

4.2.1. Stretch ratio

Calcified scaffolds stretched to higher values than the non-calcified scaffolds. The calcified scaffolds shrank on average by 50%. This implies that they would have to stretch 50% more, to reach the non contracted state of the non-calcified scaffolds. This means that for the mechanical properties of the

collagen fibres to come into effect, the collagen network first had to uncurl or unwind to the non contracted state. The calcified scaffolds had to potentially stretch more to reach the porous state of the non-calcified scaffolds. This highly stretched state of the calcified scaffolds was observed in Figure 3.26(b) & (d).

As seen in Figure 3.8, differences were observed among the calcified scaffolds where some of the scaffolds failed at much lower stretches than the rest. The variation in the concentration of calcium phosphate deposits in the volume of each scaffold could potentially be a factor. After the initial failures, the calcified scaffolds continued to stretch considerably until the final failures. As seen in the failure behaviour of the calcified scaffolds in Figure 3.20(b), some parts of the scaffold did not stretch visibly. In their corresponding Miller stains, the random network of the collagen was preserved. In the corresponding Von Kossa images 3.22, the total amount of calcium phosphate deposits were observed to be more in the parts that did not visibly stretch. It is probable that the areas of the scaffold with less calcium deposits stretched more to compensate for the areas with more calcium phosphate deposits. In the areas that did not stretch, it is likely that the calcium phosphate deposits anchored the fibres down, preventing them from stretching. In the Von Kossa Figure 3.19, the deposits seemed to form on the collagen fibres and in the SEM Figure 3.29, deposits were seen entangled in the collagen fibres. The calcified scaffolds which failed at much higher stretch values might have had a balance between the calcium phosphate deposits anchoring the fibres and creating stress concentrations. In the four scaffolds that were analysed, the amount of calcium phosphate deposits seemed to lead to higher stretches at final failure. The number of scaffolds doesn't allow for a strong confirmation of this possibility.

4.2.2. Tangential Moduli

The tangential moduli of the calcified scaffolds were significantly lower than the non-calcified scaffolds and were more compliant than the non-calcified scaffolds. This can be attributed to the fact that the calcified scaffolds had to stretch approximately 50% more. Also, the structure of the collagen fibre network was possibly affected by the cells. Hence, the overall low stiff behaviour of the calcified scaffolds can be attributed to the difference in the structure of the network.

4.2.3. Stress

The stress values at initial rupture points and final rupture points of calcified and non-calcified scaffolds were comparable. It is probable that the stresses were comparable since the collagen fibres rupturing were made of the same material. Hence, the effect of the collagen fibres was potentially the same in both types of scaffolds. Although not statistically significant, some of the calcified scaffolds did fail at lower and higher stresses than the non-calcified scaffolds. Also, a larger variation was observed in the stress values of the calcified scaffolds. Since the structure of the collagen fibres in the calcified scaffold that was not mechanically tested looked altered, it is possible that the deposits might have had some affect on lowering or raising the stresses in the scaffolds.

4.2.4. Comparing the calcified scaffolds to atherosclerotic fibrous caps

The calcified scaffolds were more compliant than the atherosclerotic fibrous caps. The studies by Loree et al [26], Holzapfel et al [27] and Teng et al [24] tested fibrous caps which exhibited high stiffness, with failures at low stretch and high stress. This high stiff behaviour is expected. A fibrous cap is a more complicated structure of varying thickness made of a dense collagen rich ECM with cells such as vascular smooth muscle cells, macrophages, immune cells and calcifications. On the other

hand, the calcified scaffold was a simplified model with a collagen fibre network, cells and calcium phosphate deposits. The fibrous cap is a much denser structure with more components in comparison to the calcified scaffolds. Even in the contracted state, the calcified scaffolds would have been more porous than a fibrous cap. The low stiffness of the calcified scaffold in comparison to the high stiff fibrous caps can be largely attributed to these differences in the composition. Also, in this study, the calcium phosphate deposits formed throughout the scaffold. However, microcalcifications identified [13, 15–17] in atherosclerotic fibrous caps were found as clusters. The distribution of microcalcifications in the cap was highly non-uniform [14]. The studies which tested fibrous caps did not examine the caps for calcifications. The caps which exhibited a high stiff behaviour in their data could have had isolated clusters of microcalcifications or large macrocalcifications. Hence, the calcified scaffolds have to be modified on the basis of their composition to imitate a fibrous cap better.

4.3. Failure

The initial failures occurred much before the final failures in the calcified scaffolds while in non-calcified scaffolds, the initial failures were closer to the final failures. In the mechanical data of the calcified scaffolds, multiple failures can be seen between the initial and final failures. Some of these failures were also observed macroscopically. In the four scaffolds analysed with their calcium phosphate deposit area fractions, the two scaffolds with higher area fractions exhibited failures between the initial and final failures in their mechanical data. Also, in the mechanical data of the calcified scaffolds, failures were also detected before the initial failure. These could be potential microscopic failures. These failures were not observed in the non-calcified scaffolds. This can potentially be explained by the calcium phosphate deposits.

A modulus mismatch exists between the stiff calcium phosphate deposits and less stiff collagen fibres. This can lead to stress concentrations. Highly localised stress can develop at interfaces between calcifications and tissue due to large dissimilarities in material properties [20]. Based on the theory of cavitation, due to these local stress concentrations, elastic energy is stored in the proximity of the microcalcifications. When the local stresses in the tissue exceeds $\approx 5/6E$, E refers to Young's modulus of tissue, theoretically this should favour rupture by the release of this stored energy in form of voids [13, 17]. It is possible that in the calcified scaffolds, during an initial failure, the collagen fibres failed due to these stress concentrations building up. This could also potentially be the reason behind the microscopic failures seen in the mechanical data. After the initial failure took place, the multiple failures that were observed till the final failures could be because of multiple stress concentrators created by the deposits causing failures. The accumulation of the micro-failures in the scaffold before the initial failures and the failures in between the initial and final failure could have led to the overall final failure of the scaffold.

Although it is probable that the calcium phosphate deposits had these effects, studying the effect of calcifications is not an easy task. There are a number of factors such as calcification size, shape, alignment, to be considered when the effect of calcifications is investigated. Even if nearly all fibrous caps have microcalcifications, only a subset of them have the potential for rupture [13]. Through biomechanical studies, microcalcifications have been predicted to increase the local stresses by a factor of 4 [13, 15–17]. The potential of microcalcifications to be stress concentrators depends on the ratio between the gap between the microcalcifications and their diameter (h/D) i.e. their proximity. This ratio, h/D has to be considered when neighbouring microcalcifications are aligned along their tensile axis. Clusters of microcalcifications with h/D<4 have been predicted to be more harmful than a single microcalcification [13]. It also depends on the shape of the microcalcifications and their pattern of distribution. Microcalcifications of the size range 5 μm to 15 μm have been pre-

dicted to increase the local stresses [13]. Since the histology of the calcified scaffolds were limited, the calcium phosphate deposits and their interaction with the collagen fibres could not be studied directly.

4.4. Overall Summary

Collagen scaffold constructs with calcium phosphate deposits were successfully cultured. These calcium phosphate deposits exhibited an elemental composition and size similar to the calcifications found in atherosclerotic fibrous caps. The calcified scaffolds exhibited a high stretch behaviour at failure. Initial failures were more pronounced in the calcified scaffolds. Multiple failures were also observed before the initial failures and between the initial and final failures. These mechanical behaviours may be attributed to the effect of the cells and calcium phosphate deposits as that was the differing factor in the calcified scaffolds. The calcified scaffolds were a less stiff than atherosclerotic fibrous caps. This was attributed to the differences in structure and composition. In this study, the initial steps towards the development of an atherosclerotic fibrous cap was achieved. To successfully imitate a fibrous cap, the composition and structure of the calcified scaffolds have to be modified to reach the mechanical properties of a real fibrous cap.

5

Concluding Remarks

5.1. Conclusion

Collagen scaffold constructs with calcium phosphate deposits to emulate an atherosclerotic fibrous cap was created. The scaffold construct was mechanically characterised and the potential effects of the cells and calcium phosphate deposits on its mechanical behaviour were investigated. The main findings of this study can be described based on the aims of the study.

1. Development of collagen scaffold constructs with calcifications:
   Collagen type 1 scaffolds were seeded with paediatric Mesenchymal Stem Cells (p-MSCs) to successfully create calcium phosphate deposits. The elemental composition and size of the calcium phosphate deposits were in line with the microcalcifications found in fibrous caps.
2. Mechanical characterisation of the collagen scaffold constructs:
   The calcified collagen scaffold constructs were mechanically tested using uniaxial tensile tests. From the tests, mechanical properties such as Cauchy stress, stretch ratio and tangential moduli were calculated. Based on these properties, the mechanical behaviour of the calcified scaffolds was described to be highly extensible and compliant. The failure behaviour was characterised by initial noticeable failures before the final failure of the scaffold, also accompanied by multiple smaller failures in between.
3. Structural characterisation of the collagen scaffold constructs:
   Through histology and scanning electron microscopy, the calcium phosphate deposits were found to form throughout the volume of the scaffold, at different concentrations. The calcium phosphate deposits seemed to form on the collagen fibres and entangled within the fibres.

5.2. Future recommendations

Based on the results of this study, the following recommendations are suggested for the continuation of this study.

1. Localised calcium phosphate deposits:
   To investigate the effect of calcium phosphate deposits on the collagen fibre network, localised calcium phosphate deposits should be created to compare the effects with regions

lacking calcium phosphate deposits. To create localised calcium phosphate deposits, localised cell seeding has to be done. This can potentially be done by seeding cells in a certain part of a scaffold and then preventing the cells from spreading to other parts by using various cues such as mechanical or chemical. This will also bring the structure of the collagen scaffold construct closer to the non-uniform distribution of microcalcification in an atherosclerotic fibrous cap. This will serve as a challenge since creating local deposits has not been done before. Seeding cells in a scaffold is already a challenge due to the dynamic nature of cells.

2. Thickness of the scaffold:
   A thickness of 65 μm in a fibrous cap of a coronary vulnerable plaque is chosen as a criterion of instability [54]. The thickness of calcified scaffolds were 1200 μm. This thickness should reduce to the thickness of a fibrous cap. This could potentially be reached by using collagen hydrogels.

3. Optimise the control:
   In this study, collagen scaffolds with no cells were used as the control. A better control would be to use collagen scaffolds, also seeded with cells but maintained in the expansion medium as long as the calcified scaffolds were maintained in the osteogenic differentiation medium. Another option would be to degrade the calcified collagen scaffolds in regions using MMPs. Another alternative would be to find a way to prevent shrinkage in the scaffolds during culture. This could possibly be done by using clamps to secure the scaffold in place while the cells are in the scaffold.

4. Optimise sectioning during histology to obtain the entire ruptured scaffolds:
   Sixteen calcified collagen scaffolds were tested in this study but due to problems faced during sectioning, only four of them could be studied effectively. To study the failure behaviour, almost the entire volume of the scaffolds should be preserved. In this study, collagen scaffolds were embedded in paraffin. A better option might be to embed the scaffolds in tissue-tek for cryostat sectioning. Embedding in tissue-tek doesn't require the processing steps required for embedding in paraffin. This also helps prevent any shrinkage caused by the dehydration steps during processing.

5. Methods to study failure behaviour:
   In this study, failure was studied through histology and scanning electron microscopy. Another effective method should be found to study the direct interface of collagen and calcifications clearly. Confocal microscopy with collagen staining could be an option.

Th calcified collagen scaffold construct made in this study can be used as a base towards the development of an in-vitro model of an atherosclerotic fibrous cap. It provides a good starting point for further research into creating the in-vitro model. Future studies should aim to further replicate the composition and mechanical properties such as the high stiff behaviour of the atherosclerotic fibrous caps and use other means such as confocal microscopy to study the interface between collagen and calcifications.

Bibliography

[1] C. Aluganti Narasimhulu, I. Fernandez-Ruiz, K. Selvarajan, X. Jiang, B. Sengupta, A. Riad, and S. Parthasarathy. Atherosclerosis — do we know enough already to prevent it? *Current Opinion in Pharmacology*, 27:92–102, 4 2016.

[2] A. Yurdagul, A. Finney, M. D. Woolard, and A. W. Orr. The Arterial Microenvironment: The Where and Why of Atherosclerosis. *Biochem J*, 473(10):1281–1295, 2016.

[3] P. Libby, J. E. Buring, L. Badimon, G. K. Hansson, J. Deanfield, M. S. Bittencourt, L. Tokgözoğlu, and E. F. Lewis. Atherosclerosis. *Nature Reviews Disease Primers*, 5(1):56, 2019.

[4] G. K. Hansson and P. Libby. The immune response in atherosclerosis: a double-edged sword. *Nat. Rev. Immunol.*, 6:508–519, 2006.

[5] L. Jonasson, J. Holm, O. Skalli, G. Bondjers, and G. K. Hansson. Regional Accumulations of T Cells, Macrophages, and Smooth Muscle Cells in the Human Atherosclerotic Plaque. *Arterioscler. Thromb. Vasc. Biol.*, 6(2):131–138, 1986.

[6] R. Nicoll and M. Henein. Arterial calcification: A new perspective? *Int. J. Cardiol.*, 228:11–22, feb 2017.

[7] E. Adiguzel, P. J. Ahmad, C. Franco, and M. P. Bendeck. Collagens in the progression and complications of atherosclerosis. *Vasc. Med.*, 14(1):73–89, 2009.

[8] F. Otsuka, K. Sakakura, K. Yahagi, M. Joner, and R. Virmani. Has Our Understanding of Calcification in Human Coronary Atherosclerosis Progressed? *Arteriosclerosis Thrombosis and Vascular Biology*, 34(4):724–736, 4 2014.

[9] A. Leszczynska, A. O'Doherty, E. Farrell, J. Pindjakova, F. J. O'Brien, T. O'Brien, F. Barry, and M. Murphy. Differentiation of Vascular Stem Cells Contributes to Ectopic Calcification of Atherosclerotic Plaque. *Stem Cells*, 34(4):913–923, 2016.

[10] A. Leszczynska and J. Mary Murphy. Vascular calcification: Is it rather a stem/progenitor cells driven phenomenon? *Frontiers in Bioengineering and Biotechnology*, 6(FEB):1–8, 2018.

[11] R. Virmani, F. D. Kolodgie, A. P. Burke, A. Farb, and S. M. Schwartz. Lessons From Sudden Coronary Death. *Arteriosclerosis, Thrombosis, and Vascular Biology*, 20(5):1262–1275, 2000.

[12] P. Libby and P. Theroux. Pathophysiology of Coronary Artery Disease The Pathophysiology of Chronic CAD. *Circulation*, 111:3481–3488, 2005.

[13] A. Kelly-Arnold, N. Maldonado, D. Laudier, E. Aikawa, L. Cardoso, and S. Weinbaum. Revised microcalcification hypothesis for fibrous cap rupture in human coronary arteries. *PNAS*, 110(26):10741–10746, 2013.

[14] N. Maldonado, A. Kelly-Arnold, D. Laudier, S. Weinbaum, and L. Cardoso. Imaging and analysis of microcalcifications and lipid/necrotic core calcification in fibrous cap atheroma. *Int J Cardiovasc Imaging*, 31:1079–1087, 2015.

[15] N. Maldonado, A. Kelly-Arnold, Y. Vengrenyuk, D. Laudier, J. T. Fallon, R. Virmani, L. Cardoso, and S. Weinbaum. A mechanistic analysis of the role of microcalcifications in atherosclerotic plaque stability: potential implications for plaque rupture. *Am J Physiol Heart Circ Physiol*, 303:619–628, 2012.

[16] Y. Vengrenyuk, S. Carlier, S. Xanthos, L. Cardoso, P. Ganatos, R. Virmani, S. Einav, L. Gilchrist, and S. Weinbaum. A hypothesis for vulnerable plaque rupture due to stress-induced debonding around cellular microcalcifications in thin fibrous caps. *PNAS*, 103(40):14678–14683, 2006.

[17] N. Maldonado, A. Kelly-Arnold, L. Cardoso, and S. Weinbaum. The explosive growth of small voids in vulnerable cap rupture; cavitation and interfacial debonding. *Journal of Biomechanics*, 46(2):396–401, 1 2013.

[18] H. Huang, R. Virmani, H. Younis, A. P. Burke, R. D. Kamm, and R. T. Lee. The Impact of Calcification on the Biomechanical Stability of Atherosclerotic Plaques. *Circulation*, 103:1051–1056, 2001.

[19] Z.-Y. Li, S. Howarth, T. Tang, M. Graves, J. U-King-Im, and J. H. Gillard. Does calcium deposition play a role in the stability of atheroma? Location may be the key. *Cerebrovascular Diseases*, 24(5):452–459, 2007.

[20] T. Hoshino, L. A. Chow, J. J. Hsu, A. A. Perlowski, M. Abedin, J. Tobis, Y. Tintut, A. K. Mal, W. S. Klug, and L. L. Demer. Mechanical stress analysis of a rigid inclusion in distensible material: a model of atherosclerotic calcification and plaque vulnerability. *Amercian Journal of Physiology-Heart and Circulatory Physiology*, 297(2):H802–H810, 8 2009.

[21] J. D. Hutcheson, C. Goettsch, S. Bertazzo, N. Maldonado, J. L. Ruiz, W. Goh, K. Yabusaki, T. Faits, C. Bouten, G. Franck, T. Quillard, P. Libby, M. Aikawa, S. Weinbaum, and E. Aikawa. Genesis and growth of extracellular-vesicle-derived microcalcification in atherosclerotic plaques. *Nature Materials*, 15(3):335–343, 2016.

[22] P. Cullen, R. Baetta, S. Bellosta, F. Bernini, G. Chinetti, A. Cignarella, A. Von Eckardstein, A. Exley, M. Goddard, M. Hofker, E. Hurt-Camejo, E. Kanters, P. Kovanen, S. Lorkowski, W. Mcpheat, M. Pentikäinen, J. Rauterberg, A. Ritchie, B. Staels, and B. Weitkamp. Rupture of the Atherosclerotic Plaque Does a Good Animal Model Exist? *Arteriosclerosis, Thrombosis, and Vascular Biology*, 23:535–542, 2003.

[23] K. H. Benam, S. Dauth, B. Hassell, A. Herland, A. Jain, K.-J. Jang, K. Karalis, H. J. Kim, L. Macqueen, R. Mahmoodian, S. Musah, Y.-S. Torisawa, A. D. Van Der Meer, R. Villenave, M. Yadid, K. K. Parker, and D. E. Ingber. Engineered In Vitro Disease Models. *Annu. Rev. Pathol. Mech. Dis*, 10:195–262, 2015.

[24] Z. Teng, Y. Zhang, Y. Huang, J. Feng, J. Yuan, Q. Lu, M. P. Sutcliffe, A. J. Brown, Z. Jing, and J. H. Gillard. Material properties of components in human carotid atherosclerotic plaques: A uniaxial extension study. *Acta Biomater.*, 10(12):5055–5063, dec 2014.

[25] A. C. Akyildiz, L. Speelman, and F. J. H. Gijsen. Mechanical properties of human atherosclerotic intima tissue. *Journal of Biomechanics*, 47:773–783, 2014.

[26] H. M. Loree, A. J. Grodzinsky, S. Y. Park, L. J. Gibson, and R. T. Lee. Static circumferential tangential modulus of human atherosclerotic tissue. *Journal of Biomechanics*, 27(2):195–204, 2 1994.

[27] G. A. Holzapfel, G. Sommer, and P. Regitnig. Anisotropic mechanical properties of tissue components in human atherosclerotic plaques. *J. Biomech. Eng. ASME*, 126(5):657–665, 2004.

[28] Z. Teng, J. Feng, Y. Zhang, M. P. F. Sutcliffe, Y. Huang, A. J. Brown, Z. Jing, Q. Lu, and J. H. Gillard. A uni-extension study on the ultimate material strength and extreme extensibility of atherosclerotic tissue in human carotid plaques. *Journal of Biomechanics*, 48:3859–3867, 2015.

[29] A. Lebedeva, D. Vorobyeva, M. Vagida, O. Ivanova, E. Felker, W. Fitzgerald, N. Danilova, V. Gontarenko, A. Shpektor, E. Vasilieva, and L. Margolis. Ex vivo culture of human atherosclerotic plaques: A model to study immune cells in atherogenesis. *Atherosclerosis*, 267:90–98, 12 2017.

[30] Y. V. Bobryshev, M. C. Killingsworth, R. S. A. Lord, and A. J. Grabs. Matrix vesicles in the fibrous cap of atherosclerotic plaque: possible contribution to plaque rupture. *Journal of Cellular and Molecular Medicine*, 12(5B):2073–2082, 2008.

[31] S. Neuss, R. Stainforth, J. Salber, P. Schenck, M. Bovi, R. Knüchel, and A. Perez-Bouza. Long-Term Survival and Bipotent Terminal Differentiation of Human Mesenchymal Stem Cells (hMSC) in Combination With a Commercially Available Three-Dimensional Collagen Scaffold. *Cell Transplantation*, 17:977–986, 2008.

[32] M.-H. Atheroma, M. P. Herman, G. K. Sukhova, P. Libby, N. Gerdes, N. Tang, D. B. Horton, M. Kilbride, and R. E. Breitbart. Expression of Neutrophil Collagenase (Matrix. *Circulation*, pages 1899–1904, 2001.

[33] E. B. Smith. The influence of age and atherosclerosis on the chemistry of aortic intima. *J. Atheroscler. Res.*, 5:241–248, 1965.

[34] A. Matrsiko, T. J. Levingstone, F. J. O'Brien, and J. P. Gleeson. Addition of hyaluronic acid improves cellular infiltration and promotes early-stage chondrogenesis in a collagen-based scaffold for cartilage tissue engineering. *J. Mech. Behav. Biomed. Mater. II*, pages 41–52, 2014.

[35] C. Ciavarella, E. Gallitto, F. Ricci, M. Buzzi, A. Stella, and G. Pasquinelli. The crosstalk between vascular MSCs and inflammatory mediators determines the pro-calcific remodelling of human atherosclerotic aneurysm. *Stem Cell Research & Therapy*, 8(99), 12 2017.

[36] C. A. Knuth, C. H. Kiernan, V. Palomares Cabeza, J. Lehmann, J. Witte-Bouma, D. ten Berge, P. A. Brama, E. B. Wolvius, E. M. Strabbing, M. J. Koudstaal, R. Narcisi, and E. Farrell. Isolating Pediatric Mesenchymal Stem Cells with Enhanced Expansion and Differentiation Capabilities. *Tissue Eng. Part C Methods*, 24(6):313–321, 2018.

[37] Y. Kupriyanova, C. Wex, S. Arndt, A. Stoll, and C. Bruns. Isotropic incompressible hyperelastic models for modelling the mechanical behaviour of biological tissues: a review. *Biomed. Eng.-Biomed. Tech*, 60(6):577–592, 2015.

[38] R. J. Hyndman and G. Athanasopoulos. Forecasting: Principles and practice. *https://otexts.com/fpp2/moving-averages.html*, 2018.

[39] A. Hayes. Moving average (ma). *https://www.investopedia.com/terms/m/movingaverage.asp*, 2019.

[40] E. Ramsden. Forecasting - the moving average. *http://www.edscave.com/forecasting—the-moving-average.html*, 2017.

[41] J. J. Mulvihill, E. M. Cunnane, S. M. Mchugh, E. G. Kavanagh, S. R. Walsh, and M. T. Walsh. Mechanical, biological and structural characterization of in vitro ruptured human carotid plaque tissue. *Acta Biomater.*, 9:9027–9035, 2013.

[42] N. Parry. How histology slides are prepared. *https://bitesizebio.com/13398/how-histology-slides-are-prepared/*, 2017.

[43] L. Cardoso, A. Kelly-Arnold, N. Maldonado, D. Laudier, and S. Weinbaum. Effect of tissue properties, shape and orientation of microcalcifications on vulnerable cap stability using different hyperelastic constitutive models. *J. Biomechancis*, 47:870–877, 2014.

[44] T. A. Mahmood, R. de Jong, J. Riesle, R. Langer, and C. A. van Blitterswijk. Adhesion-mediated signal transduction in human articular chondrocytes: the influence of biomaterial chemistry and tenascin-C. *Exp. Cell Res.*, 301(2):179–188, dec 2004.

[45] D. J. Griffon, J. P. Abulencia, G. R. Ragetly, L. P. Fredericks, and S. Chaieb. A comparative study of seeding techniques and three-dimensional matrices for mesenchymal cell attachment. *J Tissue Eng Regen Med*, 5:169–179, 2011.

[46] K. H. Vining and D. J. Mooney. Mechanical forces direct stem cell behaviour in development and regeneration. *Nat. Rev. Mol. Cell Biol.*, 18(12):728–742, dec 2017.

[47] Y.-L. Xiao, J. Riesle, and C. A. Van Blitterswijk. Static and dynamic ®broblast seeding and cultivation in porous PEO/PBT scaffolds. *J. Mater. Sci. Mater. Med.*, 10:773–777, 1999.

[48] L. A. Solchaga, E. Tognana, K. Penick, H. Baskaran, V. M. Goldberg, A. I. Caplan, and J. F. Welter. A rapid seeding technique for the assembly of large cell/scaffold composite constructs. *Tissue Eng.*, 12(7):1851–63, jul 2006.

[49] D. Dado and S. Levenberg. Cell–scaffold mechanical interplay within engineered tissue. *Semin. Cell Dev. Biol.*, 20(6):656–664, aug 2009.

[50] M. Ahearne. Introduction to cell-hydrogel mechanosensing. *Interface Focus*, 4(2):20130038, apr 2014.

[51] R. B. Roijers, N. Debernardi, J. P. M. Cleutjens, L. J. Schurgers, P. H. A. Mutsaers, and G. J. van der Vusse. Microcalcifications in early intimal lesions of atherosclerotic human coronary arteries. *Am. J. Pathol.*, 178(6):2879–87, jun 2011.

[52] I. Perrotta and E. Perri. Ultrastructural, Elemental and Mineralogical Analysis of Vascular Calcification in Atherosclerosis. *Microsc. Microanal.*, 23(5):1030–1039, 2017.

[53] D. M. Ebenstein, D. Coughlin, J. Chapman, C. Li, and L. A. Pruitt. Nanomechanical properties of calcification, fibrous tissue, and hematoma from atherosclerotic plaques. *J. Biomed. Mater. Res. PART A*, 91A(4):1028–1037, dec 2009.

[54] F. D. Kolodgie, A. P. Burke, A. Farb, H. K. Gold, J. Yuan, J. Narula, A. V. Finn, and R. Virmani. The thin-cap fibroatheroma: A type of vulnerable plaque the major precursor lesion to acute coronary syndromes. *Curr. Opin. Cardiol.*, 16(5):285–292, 2001.

A

Appendix

A.1. Matlab code for extracting stresses and stretch ratios at initial and final ruptures using slope values

```
% 1. Fitting each experimental curve with a centred moving average fit
% 2. Calculating slope over each experimental curve and extracting initial and
% final rupture point values

clear all
close all
clc
set(0, 'DefaultAxesFontName', 'times');
load('slope_initialvalues_Fitting.mat'); %loading the experimental data

a =['E119S1';'E119S2'; 'E119S3'; 'E119S4'; 'E119S5';'E119S6'; 'E120S2'; 'E120S3'; 'E120S4'; 'E120S5';
    'E122S1'; 'E122S2'; 'E122S3';'E122S4'; 'E122S5'; 'E122S6'; 'ESSca1'; 'ESSca2';'ESSca3'; 'ESSca4'; 'ESSca5'; 'ESSca6'];

%% 1. Moving average fit
index = 10;%to call the stretch and stress values from the character array individually
x = eval([a(index,:) 'SR']); %storing the stretch values in x
y = eval([a(index,:) 'CS']); %storing the stress values in y

y_filtered = movmean(y,100); %centred moving average fit over 100 sampling points

%Plotting original experimental curves
figure('Name', a(index,:));
plot(x,y,'color', [0,0,0]); grid on
legend('Original experimental data','Location','Northwest')
xlabel('Stretch Ratio');
```

```
ylabel('Cauchy Stress (MPa)');
set(gca,'FontSize',20);

%Plotting fitted experimental curves
figure('Name', a(index,:))
plot(x,y_filtered,'color', [0,0,0],'LineWidth', 1); grid on
xlabel('Stretch Ratio');
ylabel('Cauchy Stress (MPa)');
legend('Centred moving average fit','Location','Northwest');
set(gca,'FontSize',20);



%% 2. Initial and final values
% Take the corresponding x and y values from the filtered graph
% corresponding to a difference of 0.2 or more in the slope graph

slope = diff(y_filtered)./diff(x);

fittedslope = movmean(slope,100); %centred moving average fit over 100
    sampling points

%Plotting slope values with fitted curves
figure('Name', 'Slope and fit curve');
left_color = [0 0 0];
right_color = [0 0 0];
set(figure,'defaultAxesColorOrder',[left_color; right_color]);
yyaxis left
plot(x,y_filtered,'-.','color', [0,0,0],'LineWidth', 1);
ylabel('Cauchy Stress (MPa)')
hold on;
yyaxis right
ylabel('Slope')
plot(x(1:end-1),fittedslope,'color',[0.25, 0.25, 0.25]); grid on;
set(gca,'FontSize',20);

xlabel('Stretch Ratio');
legend('Centred moving average fit', 'Slope','Location','northwest')

%exporting x and y values till initial
%rupture - executing in command window based on initial points taken from
%the slope graphs
%
%i=2678; initialvalues = [x(i) y_filtered(i)];expdata=[x(1:i) y_filtered(1:i)
    ];
%j=2890; UTS values = [x(j) y_filtered(j)];expdata=[x(1:j) y_filtered(1:j)];
%i = index of initial rupture on slope, j = index of final rupture on slope
```

A.2. Matlab code for averaging over strain energy intervals

```
% 1. Calculating average values using strain energy intervals for this
% study and other studies in literature

clc
clear all
close all
%CS - Cauchy Stress, SR - Stress ratio
load('valuestillinitialrupture.mat'); %loading the stress and strain values
    until initial rupture

  a1 =['iE119S1';'iE119S2'; 'iE119S3'; 'iE119S4'; 'iE119S5';'iE119S6'; '
     iE120S2'; 'iE120S3'; 'iE120S4'; 'iE120S5';
      'iE122S1'; 'iE122S2'; 'iE122S3'; 'iE122S4';'iE122S5'; 'iE122S6'];

set(0, 'DefaultAxesFontName', 'times');

lorre1SR = xlsread('Other fibrous cap data','Sheet2', 'C3:C8');
lorre1CS  = xlsread('Other fibrous cap data','Sheet2', 'D3:D8');
lorre2SR = xlsread('Other fibrous cap data','Sheet2', 'G3:G29');
lorre2CS  = xlsread('Other fibrous cap data','Sheet2', 'H3:H29');
lorre3SR = xlsread('Other fibrous cap data','Sheet2', 'K3:K16');
lorre3CS  = xlsread('Other fibrous cap data','Sheet2', 'L3:L16');
lorre4SR = xlsread('Other fibrous cap data','Sheet2', 'O3:O20');
lorre4CS  = xlsread('Other fibrous cap data','Sheet2', 'P3:P20');
lorre5SR = xlsread('Other fibrous cap data','Sheet2', 'S3:S17');
lorre5CS  = xlsread('Other fibrous cap data','Sheet2', 'T3:T17');

  a1=['lorre1'; 'lorre2';'lorre3'; 'lorre4'; 'lorre5'];

 %% 1. Averaging over strain energy intervals for Lorree
nIntegralIntervals = 100;
xStart = 1;
resolution = 100;
SE_CS = zeros(size(a1,1),nIntegralIntervals);% allocate space for strain
    energy intervals method
SE_SR = zeros(size(a1,1),nIntegralIntervals);
figure('Name','Lorees data');
for ii = 1:size(a1,1)

    x = eval([a1(ii,:) 'SR']);
    y = eval([a1(ii,:) 'CS']);
    y=y/1000;
    xEnd = max(x);

    xGrid = linspace(xStart, xEnd, resolution);% Generate sampling points (
        row vector of resolution number of points between xStart and XEnd
    yGrid = interp1(x,y,xGrid);%, 'linear', 0);% sample data at sampling
        points
```

```
44
45      intData = cumtrapz(xGrid, yGrid);% compute cumulative integral i.e. 1 to
            each stretch
46
47      intervals = linspace(min(intData), max(intData), nIntegralIntervals); %
            generate intervals
48
49      [intDataNoDuplicates, index] = unique(intData);
50      xIntegralIntervals = interp1(intDataNoDuplicates, xGrid(index), intervals
            );
51      yIntegralIntervals = interp1(xGrid,yGrid, xIntegralIntervals);
52
53      SE_SR(ii, :) = xIntegralIntervals;
54      SE_CS(ii, :) = yIntegralIntervals;
55
56      p1 = plot(x, y,'color', [0,0,0], 'LineWidth', 1)
57      xlabel('Stretch ratio');
58      ylabel('Cauchy stress (MPa)');
59      set(gca,'FontSize',24);
60
61      hold on
62
63
64  end
65
66  EmeanSECS = mean(SE_CS);
67  EmeanSESR = mean(SE_SR);
68
69  plot(EmeanSESR,EmeanSECS,'color','r');
70
71  %% 2. Averaging over strain energy intervals for Holzapfel
72
73  %Same code as the one used for Lorre's in 1
74  %% 3.Averaging over strain energy intervals for calcified scaffolds
75
76  %Same code as the one used for Lorre's
77
78  %% 4. Teng
79  % Digisited Teng's average data directly
80
81  tengSR = xlsread('Other fibrous cap data','Teng', 'F1:F22');
82  tengCS  = xlsread('Other fibrous cap data','Teng', 'G1:G22');
83  tengCS=tengCS/1000;
84
85  %% Plotting all average graphs on one plot
86  figure('Name','All average plots');
87  set(0, 'DefaultAxesFontName', 'times');
88  p1=plot(EmeanSESR,EmeanSECS,'-','color','k','LineWidth',1);
89  hold on
```

```
90 p2=plot(hEmeanSESR,hEmeanSECS,':','color','k','LineWidth',2);
91 hold on
92 p3=plot(calmeanSESR,calmeanSECS,'-.','color','k','LineWidth',1);
93 hold on
94 p4=plot(tengSR,tengCS,'--','color','k','LineWidth',1);
95 xlabel('Stretch ratio');
96 ylabel('Cauchy stress (MPa)');
97 legend([p1 p4 p2 p3],'Loree et al,, 1994', 'Teng et al., 2014','Holzapfel et
       al., 2004','This study');
98 set(gca,'FontSize',20);
```

A.3. Derivation of stress equation for Mooney Rivlin fit

The Cauchy stress tensor in an incompressible material can be derived from a hyperelastic strain energy density function (W), which depends on I_1 and I_2, the first and second invariants of the Left Cauchy Green deformation tensor ($\underline{\underline{\mathbf{B}}}$). The stress tensor used in the derivation is shown below:

$$\underline{\underline{\sigma}} = -p\underline{\underline{\mathbf{I}}} + 2\left(\frac{\partial W}{\partial I_1} + I_1\frac{\partial W}{\partial I_2}\right)\underline{\underline{\mathbf{B}}} - 2\frac{\partial W}{\partial I_2}\underline{\underline{\mathbf{B^2}}} \tag{A.1}$$

where p is the hydrostatic pressure, $\underline{\underline{\mathbf{I}}}$ is the identity matrix, W is the strain energy density function.

The modified Mooney-Rivlin strain energy density equation is as follows,

$$W = c_1(I_1 - 3) + D_1[e^{D_2(I_1-3)} - 1] + K(J-1) \tag{A.2}$$

where W is the strain energy density, I_1 and J are the first invariant and Jacobian of the deformation gradient tensor, respectively, D_1 and D_2 are the material constants and K is Lagrange multiplier for incompressibility.

Since incompressibility is assumed, J = 1. Equation A.2 becomes,

$$W = c_1(I_1 - 3) + D_1[e^{D_2(I_1-3)} - 1] \tag{A.3}$$

Since equation A.3 only has I_1 terms, differentiating equation A.3 with respect to I_1,

$$\frac{dW}{dI_1} = c_1 + D_1D_2e^{D_2(I_1-3)} \tag{A.4}$$

Substituting equation A.4 in equation A.1:

$$\sigma = -p\underline{\underline{\mathbf{I}}} + 2c_1\underline{\underline{\mathbf{B}}} + 2D_1D_2e^{D_2(I_1-3)}\underline{\underline{\mathbf{B}}} \tag{A.5}$$

To find the hydrostatic pressure (p),

$$\sigma_{ij} = -p\delta_{ij} + 2c_1B_{ij} + 2D_1D_2e^{D_2(I_1-3)}B_{ij} \tag{A.6}$$

$$\sigma_{11} = -p + 2c_1B_{11} + 2D_1D_2e^{D_2(I_1-3)}B_{11} \tag{A.7}$$
$$\sigma_{22} = -p + 2c_1B_{22} + 2D_1D_2e^{D_2(I_1-3)}B_{22}$$
$$\sigma_{33} = -p + 2c_1B_{33} + 2D_1D_2e^{D_2(I_1-3)}B_{33}$$

1, 2 and 3 are the principal tensor directions and 1 is the loading direction. $\therefore \sigma_{22} = \sigma_{33} = 0$

$$\therefore p = 2c_1B_{22} + 2D_1D_2e^{D_2(I_1-3)}B_{22} \tag{A.8}$$

Substituting equation A.8 in A.7:

$$\sigma_{11} = -(2c_1B_{22} + 2D_1D_2e^{D_2(I_1-3)}B_{22}) + 2c_1B_{11} + 2D_1D_2e^{D_2(I_1-3)}B_{11} \tag{A.9}$$

$$= 2c_1(B_{11} - B_{22}) + 2D_1D_2e^{D_2(I_1-3)}(B_{11} - B_{22}) \tag{A.10}$$

Left Cauchy Green deformation ($\underline{\underline{\mathbf{B}}}$) can be related to the eformation gradient (F),

$$F = \begin{bmatrix} \lambda_1 & & \\ & \lambda_2 & \\ & & \lambda_3 \end{bmatrix}$$

$$B = FF^T = \begin{bmatrix} \lambda_1^2 & & \\ & \lambda_2^2 & \\ & & \lambda_3^2 \end{bmatrix}$$

$$\therefore B_{11} = \lambda_1^2, B_{22} = \lambda_2^2, B_{33} = \lambda_3^2$$

Substituting in equation A.10,

$$\sigma_{11} = 2c_1(\lambda_1^2 - \lambda_2^2) + 2D_1D_2e^{D_2(I_1-3)}(\lambda_1^2 - \lambda_2^2) \tag{A.11}$$

$\because$ Incompressibility and isotropy is assumed

$$V = \lambda_1\lambda_2\lambda_3 = 1$$

$$\because \lambda_2 = \lambda_3 = \lambda$$

$$\lambda^2\lambda_1 = 1$$

$$\lambda^2 = \frac{1}{\lambda_1^2}$$

$$I_1 = tr(B) = \lambda_1^2 + \lambda_2^2 + \lambda_3^2 \tag{A.12}$$

$$\therefore \lambda_1^2 + I_1 = 2\lambda^2 = \lambda_1^2 + \frac{2}{\lambda_1} \tag{A.13}$$

Substituting equation A.13 in A.11,

$$\boxed{\sigma_{11} = 2C_1(\lambda_1^2 - \frac{1}{\lambda_1}) + 2D_1D_2e^{D_2(\lambda_1^2+\frac{2}{\lambda_1}-3)(\lambda_1^2-\frac{1}{\lambda_1})}}$$

A.4. Matlab code for calculating Tangential Moduli

```
% 1. Mooney Rivlin fitting of calcified scaffolds
% 2. Mooney Rivlin fitting of non-calcified scaffolds
% 3. Calculating tangential moduli

clc
clear all
close all

load('valuestillinitialrupture.mat'); %loading the stress and strain values until initial rupture
a =['iE119S1';'iE119S2'; 'iE119S3'; 'iE119S4'; 'iE119S5';'iE119S6'; 'iE120S2'; 'iE120S3'; 'iE120S4'; 'iE120S5';
    'iE122S1'; 'iE122S2'; 'iE122S3'; 'iE122S4';'iE122S5'; 'iE122S6'; 'iESSca1'; 'iESSca2';'iESSca3'; 'iESSca4'; 'iESSca5'; 'iESSca6'];

%% 1 Mooney Rivlin fitting of calcified scaffolds
    C1 = zeros(16,1);
    D1 = zeros(16,1);
    D2 = zeros(16,1);
    k = 1; %index for coefficient arrays

    for ii = 1:16 %only for the calcified scaffolds

        x = eval([a(ii,:) 'SR']); %storing the stretch values in x
        y = eval([a(ii,:) 'CS']); %storing the stress values in y

        y = y*1000; %converting MPa to kPa

        % Derived mooney rivlin stress equation for modified strain energy density
        %predstress = 2*C1*(x.^2 - (1/x)) + 2*D1*D2*exp(D2*(x.^2 + (2/x) - 3))*(x.^2 - (1/x))

        [fitresult, good] = mooneyrivlinfit(x, y); %calling fit function
        allcoeff = coeffvalues(fitresult);
        C1(k) = allcoeff(1);%storing each scaffolds constants
        D1(k) = allcoeff(2);
        D2(k) = allcoeff(3);

        k = k + 1;

    end
   %% 2 Mooney Rivlin fitting of non-calcified scaffolds

    nonC1 = zeros(6,1);
    nonD1 = zeros(6,1);
    nonD2 = zeros(6,1);
    k = 1; %index for coefficient arrays
```

```
44
45      for ii = 17:22 %only for the noncalcified scaffolds for now
46
47          x = eval([a(ii,:) 'SR']); %storing the stretch values in x
48          y = eval([a(ii,:) 'CS']); %storing the stress values in y
49
50          y = y*1000; %converting MPa to kPa
51
52          % Derived mooney rivlin stress equation for modified strain energy
                density
53          %predstress = 2*C1*(x.^2 - (1/x)) + 2*D1*D2*exp(D2*(x.^2 + (2/x) - 3)
                )*(x.^2 - (1/x))
54
55          [nonfitresult, nongood] = mooneyrivlinfit(x, y); %calling fit
                function
56          nonallcoeff = coeffvalues(nonfitresult);
57          nonC1(k) = nonallcoeff(1);
58          nonD1(k) = nonallcoeff(2);
59          nonD2(k) = nonallcoeff(3);
60
61          k = k + 1;
62
63      end
64      %% Tangential Modulus
65
66  initialcalcSR = xlsread('Initial and final values with threshold value of 002
        ', 1, 'C2:C17'); %calling the initial stretch values
67  initialnoncalcSR = xlsread('Initial and final values with threshold value of
        002', 1, 'C18:C23');
68  icalTM = zeros(16,1); %to store tangential modulus at initial stretch ratio
        values for calcified
69  inoncalTM = zeros(6,1);%to store tangential modulus at initial stretch ratio
        values for non calcified
70
71  %diffstress = 2.*C1.*(2.*stretch + (1./stretch.^2))...
72      %+ 2.*D1(ii).*D2(ii).*exp(D2(ii).*(stretch.^2 + (2./stretch) - 3)).*(2.*
            stretch + (1./stretch.^2))...
73      %+ (stretch.^2 - (1./stretch)).*(2.*D1(ii).*D2(ii).*exp(D2(ii).*(stretch
            .^2 + (2./stretch) - 3))...
74      %.*2.*D2.*stretch - ((2.*D2)./stretch.^2));
75
76  % Calculating tangential modulus of calcified scaffolds
77  for ii = 1:16
78
79    % differentiated  fit stress equation
80   icalTM(ii) = 2.*C1(ii).*(2.*initialcalcSR(ii) + (1./initialcalcSR(ii).^2))
         ...
81   + 2.*D1(ii).*D2(ii).*exp(D2(ii).*(initialcalcSR(ii).^2 + (2./initialcalcSR(
         ii)) - 3)).*(2.*initialcalcSR(ii) + (1./initialcalcSR(ii).^2))...
```

```
82  + (initialcalcSR(ii).^2 - (1./initialcalcSR(ii))).*(2.*D1(ii).*D2(ii).*exp(
        D2(ii).*(initialcalcSR(ii).^2 + (2./initialcalcSR(ii)) - 3))...
83  .*2.*D2(ii).*initialcalcSR(ii) - ((2.*D2(ii))./initialcalcSR(ii).^2));
84
85  end
86  %Calculating tangential modulus of non-calcified scaffolds
87  MicalTM =icalTM/1000;
88  for ii = 1:6
89
90    % differentiated  fit stress equation
91  inoncalTM(ii) = 2.*nonC1(ii).*(2.*initialnoncalcSR(ii) + (1./initialnoncalcSR
        (ii).^2))...
92  + 2.*nonD1(ii).*nonD2(ii).*exp(nonD2(ii).*(initialnoncalcSR(ii).^2 + (2./
        initialnoncalcSR(ii)) - 3)).*(2.*initialnoncalcSR(ii) + (1./
        initialnoncalcSR(ii).^2))...
93  + (initialnoncalcSR(ii).^2 - (1./initialnoncalcSR(ii))).*(2.*nonD1(ii).*
        nonD2(ii).*exp(nonD2(ii).*(initialnoncalcSR(ii).^2 + (2./initialnoncalcSR
        (ii)) - 3))...
94  .*2.*nonD2(ii).*initialnoncalcSR(ii) - ((2.*nonD2(ii))./initialnoncalcSR(ii)
        .^2));
95
96  end
97  MinoncalTM = inoncalTM/1000. %converting to MPa
98  % Box plots of initial stretch ratio values
99       xinitial = [MicalTM; MinoncalTM];
100      g1 = repmat({'First'},[size(MicalTM),1]);
101      g2 = repmat({'Second'},[size(MinoncalTM),1]);
102      g = [g1; g2];
103      figure('Name', 'Tangential modulus at Initial rupture points');
104      p1 = boxplot(xinitial,g,'Notch','off','Labels',{'Calcified scaffolds','
           Non-calcified scaffolds'},'Whisker',1);
105      ylabel('Tangential Modulus (MPa)'); ylim([0 0.8]);
106      set(gca,'FontSize',18);
107
108 %Extracting quartile and median values
109 icalTMval = quantile(MicalTM,[.25 .5 .75]);
110 inoncalTMval = quantile(MinoncalTM,[.25 .5 .75]);
```

A.5. Miller stains of non-calcified scaffolds

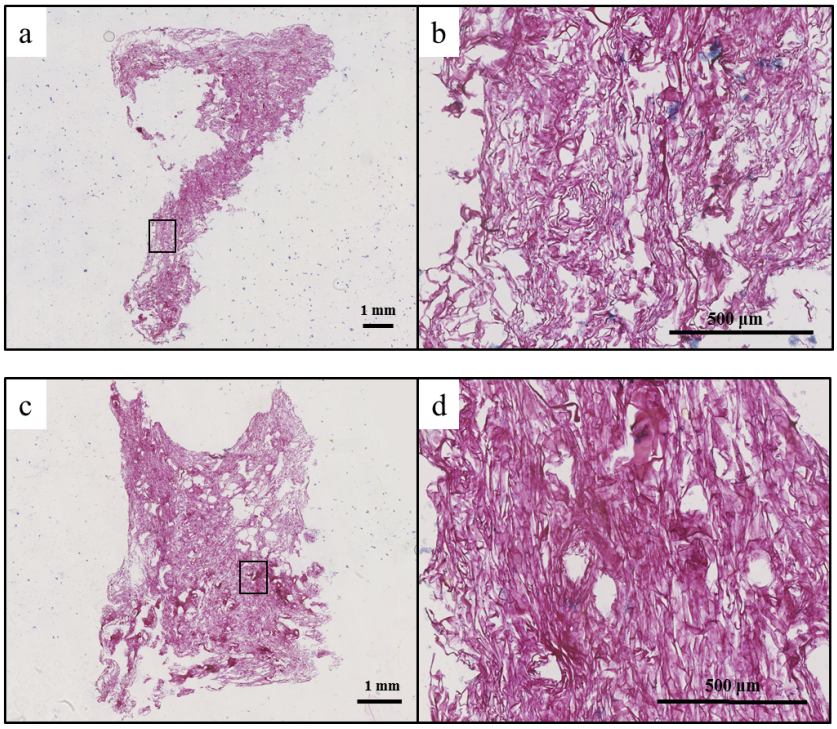

Figure A.1: (a) & (c) Overview images of Miller stains of two non-calcified scaffolds, (b) & (c) Images at a higher magnification of the marked regions

A.6. Scanning Electron Microscopy line analysis

An example of a line analysis carried out on an area of the calcified scaffold through energy dispersive x-ray spectroscopy (EDX).

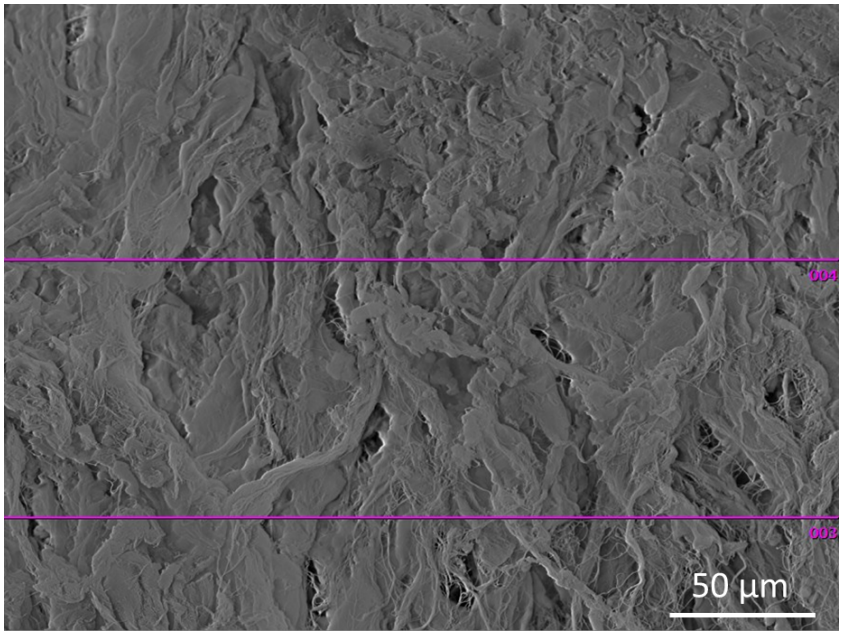

Figure A.2: Scanning Electron Microscopy image of an area over which two line analyses were carried out using energy dispersive x-ray spectroscopy (EDX).

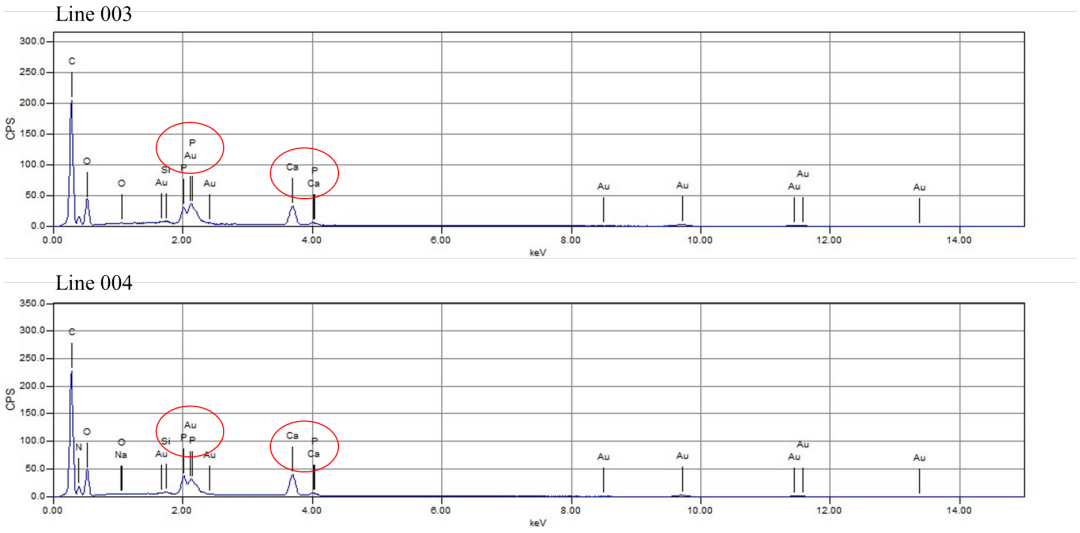

Figure A.3: The corresponding spectra of the line analyses with the Ca and P peaks marked with red circles.